New measurements of low-energy resonances in the ^{22}Ne(p,γ)^{23}Na reaction

K. J. Kelly, A. E. Champagne, L. N. Downen, J. R. Dermigny, S. Hunt, C. Iliadis, and A. L. Cooper

Phys. Rev. C **95**, 015806 — Published 19 January 2017

DOI: 10.1103/PhysRevC.95.015806

New Measurements of Low-Energy Resonances in the ^{22}Ne(p,γ)^{23}Na Reaction

K. J. Kelly[1,2ab], A. E. Champagne[1,2], L. N. Downen[1,2],
J. R. Dermigny[1,2], S. Hunt[1,2], C. Iliadis[1,2], and A. L. Cooper[1,2]
[1] *Department of Physics and Astronomy, University of North Carolina at Chapel Hill, Chapel Hill, NC 27599-3255, USA and*
[2] *Triangle Universities Nuclear Laboratory, Duke University, Durham, NC 27708-0308, USA*
(Dated: December 7, 2016)

The ^{22}Ne(p,γ)^{23}Na reaction is one of the most uncertain reactions in the NeNa cycle and plays a crucial role in the creation of ^{23}Na, the only stable Na isotope. Uncertainties in the low-energy rates of this and other reactions in the NeNa cycle lead to ambiguities in the nucleosynthesis predicted from models of thermally pulsing AGB stars. This in turn complicates the interpretation of anomalous Na-O trends in globular cluster evolutionary scenarios. Previous studies of the ^{22}Ne(p,γ)^{23}Na, ^{22}Ne(^{3}He,d)^{23}Na, and ^{12}C(^{12}C,p)^{23}Na reactions disagree on the strengths, spins, and parities of low-energy resonances in ^{23}Na and the direct-capture ^{22}Ne(p,γ)^{23}Na reaction rate contains large uncertainties as well. In this work we present new measurements of resonances at $E_r^{c.m.}$ = 417, 178, and 151 keV and of the direct-capture process in the ^{22}Ne(p,γ)^{23}Na reaction. The resulting total ^{22}Ne(p,γ)^{23}Na rate is approximately a factor of 20 higher than the rate listed in a recent compilation at temperatures relevant to hot bottom burning in AGB stars. Although our rate is close to that derived from a recent ^{22}Ne(p,γ)^{23}Na measurement by Cavanna *et al.* (2015), we find that this large rate increase results in only a modest 18% increase in the ^{23}Na abundance predicted from a 5 $M_\odot$ thermally pulsing AGB star model from Ventura & D'Antona (2005). The estimated astrophysical impact of this rate increase is in marked contrast to the factor of $\sim$3 increase in ^{23}Na abundance predicted in Cavanna *et al.* (2015) and is attributed to the interplay between the ^{23}Na(p,α)^{20}Ne and ^{20}Ne(p,γ)^{21}Na reactions, both of which remain fairly uncertain at the relevant temperature range.

PACS numbers: 25.40.Lw,26.20.Cd,27.30.+t

[a] Corresponding Author
[b] Present Address: Los Alamos National Laboratory, Los Alamos, NM 87545

I. INTRODUCTION

Globular clusters contain some of the oldest stars in existence and provide an estimate for the age of the galaxy and a lower limit on the age of the universe [1]. Furthermore, globular clusters are thought to represent ideal stellar laboratories because they contain a coeval population of stars of the same initial metallicity and exhibit nearly every stage of stellar evolution [2] in a single region of space. Observations of multiple main sequences and anomalous elemental abundance anti-correlations in cluster stars indicate that globular clusters are much more complicated than this simple picture suggests however. Excellent examples of both of these phenomena in globular cluster NGC 2808 can be found in Refs. [3, 4]. Comprehensive reviews of this topic can be found in Refs. [1, 2, 5].

An anti-correlation between sodium and oxygen is a ubiquitous feature of globular clusters, but is not observed in field stars. Thus it must arise from the cluster environment. This effect requires simultaneous operation of the NeNa and CNO cycles at temperatures beyond what is expected for many stars that display the anti-correlation [6]. These observations, among others, have led to the idea that abundance anomalies arise from self-enrichment of the globular cluster interstellar medium [7, 8]. Suggested self-enrichment sources include winds from asymptotic giant branch (AGB) stars [9, 10], winds from fast-rotating massive stars [4, 11], and massive binaries [12]. Anomalously high helium abundances in stars with extreme oxygen depletion have also led to the supposition of a "deep extra mixing" episode in RGB stars that exhibit an elevated He abundance [13, 14]. However, it is clear from abundance variations in main sequence stars that an extra RGB mixing process cannot be solely responsible for the observations [5].

The successes and drawbacks of each of these scenarios are summarized in Refs. [5, 12], but it is argued [5, 14] that the AGB stellar wind scenario appears to be the most likely. AGB stars massive enough to undergo hot-bottom burning (HBB) during thermal pulses are required to produce significant sodium abundances in the envelope prior to the planetary nebula phase [15]. Models of a 5 $M_{\odot}$ AGB star from Ref. [16] show that temperatures at the base of the convective envelope, which are important for HBB, can be 0.098 GK ($T_9 = 0.098$) on average, with a maximum of $T_9 = 0.11$. The NeNa and MgAl cycles are active in this temperature range.

Because ^{23}Na is the only stable sodium isotope, the rates of the reactions involved in the creation and destruction of ^{23}Na must be precisely and accurately known in order to eliminate nucleosynthetic ambiguities. Cesaratto *et al.* [17] recently investigated the ^{23}Na(p,γ)^{24}Mg reaction rate and its relation to the destruction of ^{23}Na in AGB stars. In that work, it was determined that the sodium abundances in AGB stars are insensitive to variations of the ^{23}Na(p,γ)^{24}Mg reaction rate within its present uncertainties at the relevant temperature range. However, strong correlations between the ^{23}Na abundance and variations of the ^{23}Na(p,α)^{20}Ne, ^{20}Ne(p,γ)^{21}Na, and ^{22}Ne(p,γ)^{23}Na reaction rates within their respective uncertainties were found.

Although variations of the ^{22}Ne(p,γ)^{23}Na reaction rate were shown to have the smallest effect on the final ^{23}Na abundance of these three reactions, the rate for that reaction was calculated using spectroscopic factors reported from measurements of the ^{22}Ne(^{3}He,d)^{23}Na reaction by Hale et al. [18, 19]. Specifically, this included a strength of $\omega\gamma(\mathrm{E}_r^{c.m.} = 151\ \mathrm{keV}) = 9.2{\times}10^{-9}$ eV for the 151-keV resonance in ^{22}Ne(p,γ)^{23}Na, which resulted from L = 3 transfer in (^{3}He,d) with a spectroscopic factor of $(2\mathrm{J}_f + 1)\mathrm{C}^2\mathrm{S} = 9.2{\times}10^{-3}$. This L-assignment was based on a tabulated [20] spin-parity of $\mathrm{J}^{\pi} = 7/2^-$ for this resonance. More recent work by Jenkins *et al.* [21] indicates that this resonance may actually be a doublet of states, one with $\mathrm{J}^{\pi} = 7/2^-$ and another with a tentative $\mathrm{J}^{\pi} = 3/2^+$. With regard to the resonance at $\mathrm{E}_{c.m.} = 178$ keV, Ref. [22] adopted $\omega\gamma(178) \leq 2.6{\times}10^{-6}$ eV from Refs. [18, 19]. Fig. 1 shows the placement of these resonances with respect to the Gamow window, the energy range over which the majority of thermonuclear reactions occur for a particular stellar environment, corresponding to the 5 $\mathrm{M}_{\odot}$ AGB stellar model of Ref. [16] (shown as the shaded region). Given the questionable assumptions on which these results were based, new direct measurements of these resonances and other important contributions to the total ^{22}Ne(p,γ)^{23}Na reaction rate are warranted.

A preliminary measurement [24] of the ^{22}Ne(p,γ)^{23}Na reaction indicated that the strength of the resonance at $\mathrm{E}_r^{c.m.} = 178$ keV is $\omega\gamma(178\ \mathrm{keV}) \geq 1.2{\times}10^{-7}$ eV. This lower limit was calculated assuming that 100% and 92% of the decay strength passes through the $\mathrm{E}_x = 440$-keV and 2076-keV states, respectively. Note that a 100% branch to the 440-keV state is internally inconsistent with population of the 2076-keV state since the latter has an 8.2% branch to the ground state [25], bypassing the 440-keV state.

More recently Cavanna *et al.* [26] reported strengths for the 178- and 151-keV resonances of $\omega\gamma(178\ \mathrm{keV}) = 1.87(6){\times}10^{-6}$ eV and $\omega\gamma(151\ \mathrm{keV}) = 1.48(10){\times}10^{-7}$ eV. The quoted values are said to include both systematic and statistical uncertainties. However, a comparison of the 3.2% total uncertainty in $\omega\gamma(178\ \mathrm{keV})$ to the reported systematic uncertainties of 3%, 1.1%, and 1% in the γ-ray detection efficiency, effective gas density, and beam charge, respectively (yielding a net systematic uncertainty of 3.3% when added in quadrature) implies an essentially negligible statistical uncertainty. This seems inconsistent with the statistics of their published γ-ray spectrum. No spectrum of the 151-keV resonance was included in that work, making a similar comparison difficult. A more detailed discussion

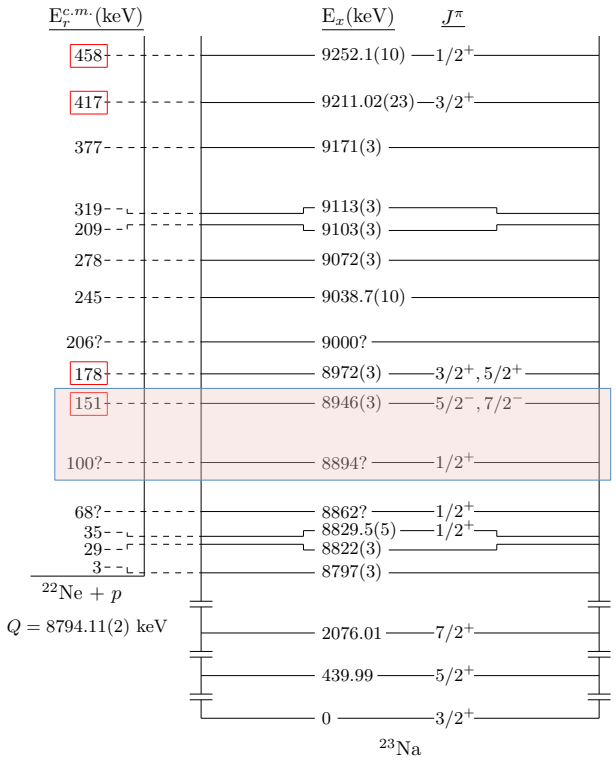

FIG. 1: A diagram of resonant levels in ^{23}Na in the energy range evaluated in this work. All known spin-parities are listed. The energy, spin, and parity of the levels shown as well as the Q-value of the ^{22}Ne(p,γ)^{23}Na reaction are from Ref. [23]. The center-of-mass interaction energies of the resonances investigated in this work are enclosed in the red boxes. Additionally, the direct-capture reaction rate was measured just below the 417-keV resonance.

of the results of Ref. [26] will be presented in Sec. IV.

In this work, we report on new measurements of the ^{22}Ne(p,γ)^{23}Na resonances at $E_r^{c.m.}$ = 417, 178, and 151 keV. We have also measured the direct-capture (DC) component of the cross section at E_p^{lab} = 425 keV. Data were analyzed using the TFractionFitter [27] class of ROOT [28] as well as with a Markov-chain Monte Carlo (MCMC) adaptation of the same data-analysis technique [29]. The strength of the ^{22}Ne(p,γ)^{23}Na resonance at $E_r^{c.m.}$ = 458 keV was recently revised by Refs. [30, 31] and is known to high precision. All resonance strengths and DC cross sections reported in this work were measured relative to this resonance.

II. EXPERIMENTAL EQUIPMENT

A. ACCELERATORS

We measured the^{22}Ne(p,γ)^{23}Na reaction at the Laboratory for Experimental Nuclear Astrophysics (LENA), located at the Triangle Universities Nuclear Laboratory. Measurements at $E_{lab} < 200$ keV were carried out using the electron cyclotron resonance ion source (ECRIS) accelerator, which is designed to provide proton beams with a long-term average beam current of ∼1.2 mA on target and a maximum beam current of ∼2.0 mA [32]. During our measurements, average currents of up to 2.22 mA were achieved. A 1 MV model JN Van de Graaff accelerator was used to provide higher-energy beams, with a maximum beam current of ∼120 μA and a 1–3 keV spread in beam energy. The energy calibration for both accelerators was established to < 1 keV by using well-known resonances in the reactions ^{18}O$(p,\gamma)^{19}$F, ^{26}Mg$(p,\gamma)^{27}$Al, and ^{27}Al$(p,\gamma)^{28}$Si [33]. For more details on the LENA facility, see Ref. [33].

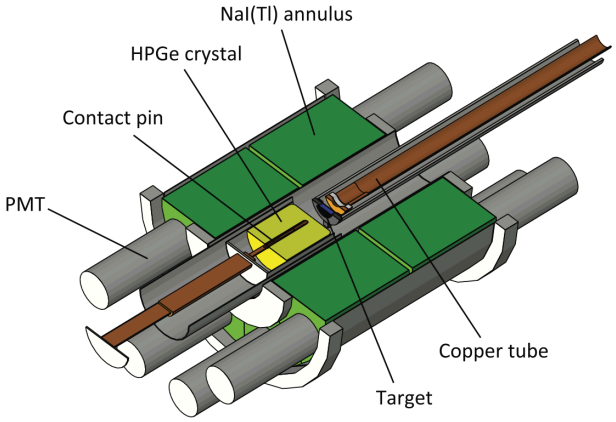

FIG. 2: (color online) The LENA $\gamma\gamma$-coincidence spectrometer. Original figure from Ref. [32].

B. DETECTORS

The γ rays emitted from the target were analyzed with a 135% relative efficiency coaxial high-purity germanium (HPGe) detector as well as a 16-segment NaI(Tl) annulus. These detectors comprise the LENA $\gamma\gamma$-coincidence spectrometer described in Refs. [17, 32, 34, 35] and shown in Fig. 2. These detectors were surrounded on all six sides by 1.27-cm thick lead panels and by five 5-cm thick plastic scintillator paddles, which were used to veto spurious events induced by cosmic-ray muons. The HPGe detector was placed 1.1 cm from the target at 0^{o} relative to the beam direction during data acquisition. This technique has been demonstrated to reduce low-energy environmental background by approximately two orders of magnitude [17, 32, 34, 35].

Coincidence spectra were obtained by requiring a time difference of $\Delta t \approx 50$ ns between the arrival of HPGe and NaI signals. This timing window is intentionally large compared to the typical time between the emission of γ rays in a cascade to account for the possibility of long mean lifetimes of poorly-known resonances studied in this work. Additionally, a summed HPGe–NaI energy requirement was enforced. Typically, this energy gate is chosen to be a trapezoidal gate specified by

$$\mathrm{E}_{\mathrm{min}}^{\mathrm{total}} \leq \mathrm{E}_{\mathrm{NaI}} + \mathrm{E}_{\mathrm{HPGe}} \leq \mathrm{E}_{\mathrm{max}}^{\mathrm{total}}. \quad (1)$$

This type of coincidence energy gate was employed during the analysis of all data except those data collected on the 151-keV resonance. These data required a carefully-chosen coincidence energy gate that will be discussed in more detail in Sec. IV D. The maximum HPGe–NaI γ-ray energy sum for those data sets analyzed via a trapezoidal gate, $\mathrm{E}_{\mathrm{max}}^{\mathrm{total}}$, varied between 9.1 and 10.0 MeV depending on the maximum expected γ-ray energy from the reaction of interest. The minimum HPGe–NaI γ-ray energy sum, $\mathrm{E}_{\mathrm{min}}^{\mathrm{total}}$, varied between 2.8 and 3.5 MeV depending on which gate produced the best signal-to-background ratio for low-energy peaks of interest in a particular data set. All timing and energy information was analyzed with NIM and VME standard electronics modules during data acquisition. Coincidence gates were applied in a post-processing step using the data-acquisition software JAM [36].

The data-analysis method employed in this work is described in Sec. III and relies on GEANT simulations of the spectrometer employed here. The critical dimensions of the HPGe crystal were measured with a CT scan of the detector [37]. Past studies of the HPGe detector have included extensive GEANT simulations comparing experimentally measured and simulated γ-ray spectra of radioactive sources including ^{60}Co, ^{56}Co, and ^{137}Cs as well as (p,γ) resonances in ^{14}N, ^{18}O, ^{23}Na, and ^{27}Al target nuclei [17, 34, 38]. Comparisons similar to those carried out for the HPGe have been completed for the NaI using ^{60}Co, the 151-keV resonance in the $^{18}\mathrm{O}(p,\gamma)^{19}\mathrm{F}$ reaction [35], and both resonant and DC spectra from the $^{17}\mathrm{O}(p,\gamma)^{18}\mathrm{F}$ reaction [32]. Finally, a comparison of singles and coincidence measurements of the 458-keV resonance in the $^{22}\mathrm{Ne}(p,\gamma)^{23}\mathrm{Na}$ reaction discussed in Ref. [39] was shown to give nearly identical results between the two detection modes. The accuracy of the GEANT simulation of the LENA $\gamma\gamma$-coincidence detection system is further verified in Sec. IV A.

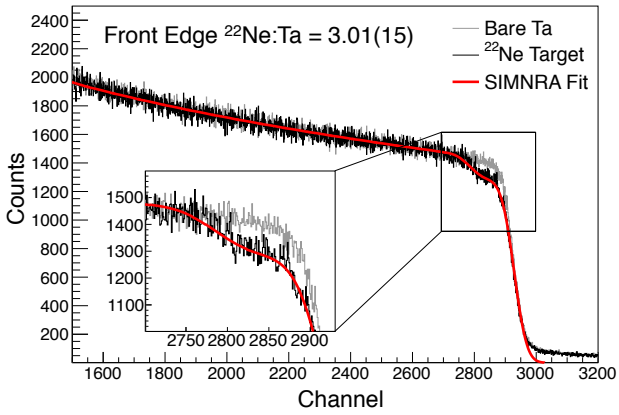

FIG. 3: (color online) An example RBS spectrum obtained by measuring α particles backscattered from a 6.5-keV thick ^{22}Ne target is shown in black. A bare tantalum spectrum is shown in gray and a fit to the ^{22}Ne target data is shown in red. The fit was calculated using the program SIMNRA [41]. A single layer of ^{22}NeTa in an approximately 1:3 stoichiometry was added onto an infinitely thick Ta sample in SIMNRA was used to obtain the fit to the data.

C. TARGETS

Targets were fabricated using the Eaton Ion Implanter located at the University of North Carolina at Chapel Hill. Singly ionized ^{22}Ne atoms were implanted into 0.5-mm thick tantalum target backings. Prior to implantation, these backings were chemically etched [40] and resistively heated to remove contaminants. Targets of two different thicknesses were required, one for each type of cross section measured in this work. Relatively thick targets were desired for on-resonance measurements to ensure that a yield consistent with that from an infinitely-thick target would be observed. Thinner targets were advantageous for DC measurements because of potential contamination from ^{22}Ne(p,γ)^{23}Na resonances below the proton beam energy and also because thin targets minimize the variation in the DC interaction energy across the thickness of the target. Thus, ion implantation energies of 25 and 100 keV were used to produce 6.5- and 21-keV thick targets $E_p^{c.m.} = 458$ keV, respectively. A dose of ∼100-140 μA·hrs was supplied for each target, which is well in excess of the required saturation dose for targets of our measured thickness and stoichiometry.

The initial target stoichiometry was measured via Rutherford Backscattering Spectrometry (RBS) to be ^{22}Ne:Ta = 1:3.01(15) for targets of both thicknesses. An example RBS spectrum obtained on an unused 6.5-keV thick target is shown in Fig. 3 along with a fit to the experimental spectrum calculated using the simulation program SIMNRA [41]. Typical excitation curves over the 458-keV resonance in ^{22}Ne(p,γ)^{23}Na for unused thick and thin targets are shown in red in Figs. 4 & 5, respectively.

The targets were observed to degrade considerably during data acquisition. Thick targets displayed a decrease of approximately 35% in the height of the yield curve after 10 C of charge had been collected on target while thin targets displayed a similar level of target degradation after 6 C. The black diamonds on Figs. 4 & 5 show yield curves taken after 10 C for thick targets and 6 C for thin targets. Additionally, a typical trend of the maximum measured yield on the 458-keV center-of-mass resonance versus accumulated beam charge on a target used for on-resonance data acquisition is shown in Fig. 6. Note the initial sharp decrease in the observed maximum yield followed by a relatively constant maximum yield for approximately 4 C. Subsequently, the maximum yield steadily decreases again, typically after the accumulation of approximately 8-12 C on target. These thicker targets were deemed unusable after approximately 8-12 C while thinner targets were discarded after ∼6 C, depending on the observed target degradation. As a consequence of this relatively short target lifetime, a total of 33 implanted ^{22}Ne targets were used during the course of this work.

An observed decrease in the maximum yield of a resonance yield curve corresponds to a decrease in the number density of ^{22}Ne atoms within the tantalum lattice, n_{22}, with accumulated beam charge. However, the quantity that will ultimately be used in calculations of resonance strengths and DC cross sections is the stopping cross section of the ^{22}Ne-Ta combination in the center-of-mass frame, ϵ_{eff}. This quantity is related to n_{22} through the relation [42]

$$\epsilon_{eff}^{c.m.} = \frac{\Delta E}{n_{22}}, \tag{2}$$

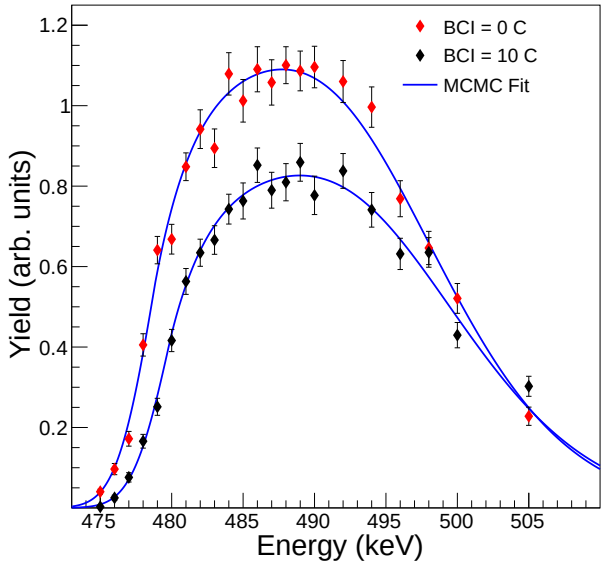

FIG. 4: (color online) Typical yield curve of a ^{22}Ne target used for on-resonance data acquisition before and after 10 C of accumulated beam charge shown as red and black diamonds, respectively.

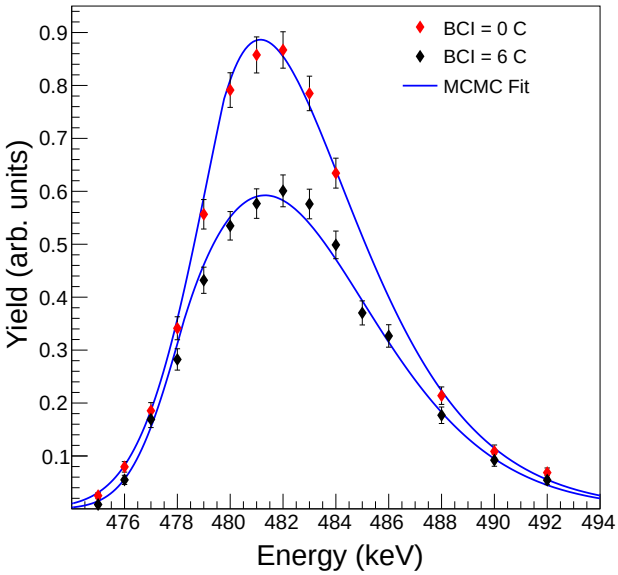

FIG. 5: (color online) Typical yield curve of a ^{22}Ne target used for DC and off-resonance data acquisition before and after 6 C of accumulated beam charge shown as red and black diamonds, respectively.

where ΔE is the energy loss in the center-of-mass frame. The quantity n_{22} can also be written as

$$n_{22} = \frac{2}{\lambda_r^2}\frac{A_y}{\omega\gamma}. \tag{3}$$

The parameters λ_r, A_y, and $\omega\gamma$ are the deBroglie wavelength, the area under the yield curve, and the resonance

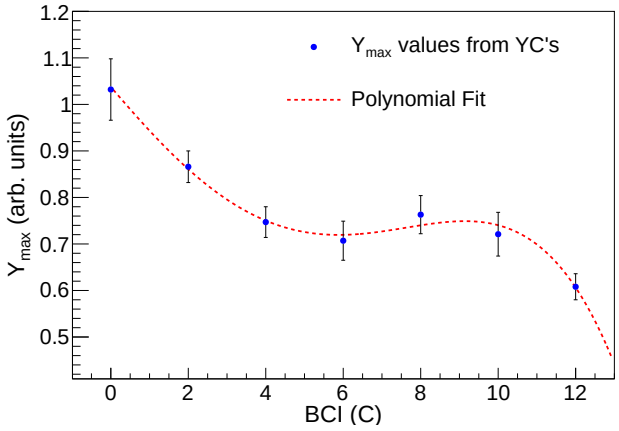

FIG. 6: (color online) A typical trend of target degradation versus accumulated beam charge for the thick targets used during on-resonance data acquisition. In general, these targets were observed to show an initial decrease in maximum resonance yield over the first ∼4 C accumulated on target, followed by ∼4 C of approximately constant maximum yield, and finally a further drop in the maximum yield. The polynomial fit to this trend, shown as the red dashed line, was compared to as a check on the accuracy of the average Y_{max} values before and after a particular data-acquisition period.

strength, respectively. The yield-curve area can be calculated via

$$A_y = \frac{\Delta E Y_{max} f_{SC}}{B \eta_p W}, \tag{4}$$

where Y_{max} is the maximum yield of the γ ray being analyzed, f_{SC} is a coincidence-summing correction factor, calculated according to the methods of Ref. [30], and B and η_p are the branching ratio and detector full-energy peak efficiency associated with the γ ray of interest. The parameter W corrects for the angular distribution of the γ ray. Substituting Eqs. 3 & 4 into Eq. 2, we obtain

$$\epsilon_{eff}^{c.m.} = \Delta E \left[\frac{\lambda_r^2}{2} \frac{\omega\gamma}{A_y} \right] = \omega\gamma \left(\frac{\lambda_r^2}{2} \right) \frac{B \eta_p W}{Y_{max} f_{SC}}. \tag{5}$$

Note that ΔE cancels out of this equation. The quantity $\epsilon_{eff}^{c.m.}$ is related to the target stoichiometry via the relation

$$\epsilon_{eff}^{c.m.} = \left(\frac{m_{22}}{m_{22} + m_p} \right) \left[\epsilon_{22}^{lab} + \left(\frac{n_{\rm Ta}}{n_{22}} \right) \epsilon_{\rm Ta}^{lab} \right], \tag{6}$$

where m_{22} is the mass of ^{22}Ne and ϵ_{22}^{lab} and $\epsilon_{\rm Ta}^{lab}$ are the ^{22}Ne and Ta stopping cross sections in the laboratory frame, calculated using SRIM [43] at the relevant interaction energy. Solving Eq. 6 for the target stoichiometry yields

$$\frac{n_{Ta}}{n_{22}} = \frac{1}{\epsilon_{\rm Ta}^{lab}} \left[\left(\frac{m_{22} + m_p}{m_{22}} \right) \epsilon_{eff}^{c.m.} - \epsilon_{22}^{lab} \right]. \tag{7}$$

Eqs. 5 & 7 can be used to obtain the target stoichiometry at any stage of target degradation.

This method for obtaining the stopping cross section at the desired interaction energy works well for targets that do not degrade during data acquisition. This is clearly not the case for the ^{22}Ne targets used in this work. If a data set required more than ∼1 C of accumulated beam charge, then target-degradation effects must be taken into account. Given that Y_{max} is the only parameter in Eq. 5 that varies as the target degrades, the effects of target degradation were accounted for in the following way: a yield curve across the 458-keV resonance was taken on every target prior to its use, followed by a yield curve after every 2-5 C of accumulated beam charge on target. Yield curves were taken after every 2 C for the first 120 C of total accumulated beam charge on thick ^{22}Ne targets until it was determined that the effects of this target degradation were understood. This 2 C interval was extended to ∼3 C across the 65 C subsequently accumulated on thin targets and to 5 C for the 30 C taken with thick targets on the 178-keV resonance. It should be noted that the ratio of A_y/ΔE, which provides an alternative measure of the maximum resonance yield

independent of the resonance width or particle energy loss, was found to be in agreement with the calculated Y_{max} values and also decreased at essentially the same rate as the maximum yield.

Each yield curve was fit via the Markov-chain Monte Carlo algorithm [32, 44] mentioned earlier in this section in order to obtain the Y_{max} associated with each yield curve, which was then used to derive $\epsilon_{eff}^{c.m.}$ via Eq. 5. The $\epsilon_{eff}^{c.m.}$ values calculated before and after every interval of accumulated beam charge were averaged to obtain an average stopping cross section for that portion of the total data set, ϵ_{eff}^{avg}. Finally, these average stopping cross section values were used in an average of the stopping cross section over the course of an entire data set, weighted by the accumulated charge (BCI) via the relation

$$\epsilon_{eff}^{BCI} = \frac{\sum_i \epsilon_{eff,i}^{avg} N_{p,i}}{\sum_j N_{p,j}}, \tag{8}$$

where the indices i and j refer to each data acquisition period and $N_{p,i}$ is the number of protons accumulated during data acquisition period i. Any data set that required more than $\sim$1 C of beam on target required a BCI-weighted stopping cross section calculated according to Eq. 8 to be incorporated into the final result. Note that this kind of weighted average assumes equal uncertainties for all ϵ_{eff}^{avg} and $\epsilon_{eff}^{c.m.}$ values. Also, the uncertainty in the resulting value of ϵ_{eff}^{BCI} is not lower than the uncertainties of ϵ_{eff}^{avg} and $\epsilon_{eff}^{c.m.}$, as would occur in a typical weighted average. The net uncertainty in the ϵ_{eff}^{BCI} for a particular data set changed depending on the total amount of beam charge required for a particular data set. These uncertainties will be summarized with the rest of the uncertainty budget at the end of Sec. III C.

III. DATA ANALYSIS

A. Standard TFractionFitter Routine

Data from 417-keV resonance and from DC measurement at $E_p^{lab} = 425$ keV were analyzed according to the method described in Refs. [32, 45] and further detailed in Ref. [30]. All resonant decays previously reported in the literature, as well as unobserved potential L = 1 transitions were simulated with the GEANT Monte Carlo simulation package (version 4.9.6) [46]. For the DC measurements, only transitions to levels in ^{23}Na that have known secondary decays and have been previously reported in the literature were considered. Direction-direction correlations were calculated according to Refs. [39, 42, 47] and incorporated into the all simulations. The energy resolution of the detector was measured as a function of γ-ray energy by populating the $E_r^{c.m.} = 259$ keV resonance in the ^{14}N$(p,\gamma)^{15}$O reaction. This resolution function was applied to each simulation.

These potential resonant/DC decay simulations were then treated as "templates" for a fit to the experimental data. Included with these templates were simulations of expected beam-induced backgrounds, arising from the ^{11}B$(p,\gamma)^{12}$C and ^{12}C$(p,\gamma)^{13}$N reactions, and a measured spectrum of environmental and cosmic-ray background radiation. All of these templates were then used in a binned log-likelihood maximization fitting routine, as described in Ref. [27]. This procedure differs from traditional likelihood maximization routines in that statistical variations in the data as well as in the Monte Carlo-generated and experimentally-measured template histograms are taken into account.

The results of this fitting routine are the parameters, F_j, defined to be the fraction of the experimental spectrum accounted for by template j. Given that the number of reactions simulated with GEANT for a particular template, N_j^{sim}, is known, the F_j can be used to calculate the number of reactions corresponding to that template present within the data, N_j^{data} (also referred to as the partial number of reactions for template j) using the equation

$$N_j^{data} = \frac{A_{total}^{data}}{A_j^{sim}} F_j N_j^{sim}, \tag{9}$$

where A_{total}^{data} is the total area of the experimental data spectrum and A_j^{sim} is the total area of the simulated spectrum for template j. It is then a simple task to calculate the total number of reactions observed in the experimental data spectrum, N_R^{data}, by summing over the partial numbers of reactions for each decay cascade

$$N_R^{data} = \sum_{j=0}^{m} N_j^{data}. \tag{10}$$

The quantity N_R^{data} is the parameter most relevant to reaction cross sections. These parameters are related to B(R/DC→E_j), the branching ratio for the decay to the state with energy E_j, via the relation

$$B(R/DC \rightarrow E_j) = N_j^{data}/N_R^{data}. \tag{11}$$

The advantages of this data-analysis method are described in Refs. [30, 32, 45]. The most notable advantages are that there is no need to subtract background or to correct the data for coincidence-summing effects. Both contributions are already accounted for: Background templates are included in the fit, as mentioned above, and coincidence summing is automatically modeled by the GEANT simulations. Finally, this analysis technique allows the user to consider not just the full-energy peaks of interest, but also the escape peaks and Compton continuum that compose up to ∼95% of the spectrum.

B. Markov-Chain Monte Carlo TFractionFitter Routine

The data-analysis method described in Sec. III A has been shown to be successful in determining high-precision branching ratios and total numbers of reactions associated with both direct-capture and resonance reactions [30, 32, 45]. However, in the event that a signal from one or more decay branches is too weak to be confidently identified via the method of Sec. III A an upper limit for the value in question must be reported. This situation was encountered in analyzing data from the 178- and 151-keV resonances (described in Secs. IV C & IV D), which are both orders of magnitude weaker than the resonances at $E_r^{c.m.} = 458$ and 417 keV.

This issue can be addressed by adapting the above-described TFractionFitter methodology to a Bayesian Markov-chain Monte Carlo (MCMC) sampling routine. This approach is described in detail in Ref. [29] so here we will only provide a brief description of the important differences between this method and that of Sec. III A.

The primary change to note when discussing the MCMC TFractionFitter routine is that the fractions, F_j, of the total area of the data spectrum accounted for by the templates j are no longer calculated using the MINUIT library [48]. Instead, the same log-likelihood function shown in Ref. [27] is used in the definition of a multivariate, joint posterior distribution, P($\hat{F}$|D). This distribution is proportional to

$$P(\hat{F}|D) \sim P(\hat{F}) \ln(\mathscr{L}), \tag{12}$$

where $\ln(\mathscr{L})$ is the log-likelihood function of Ref. [27] and P($\hat{F}$) is the joint prior probability function for the model parameters. An initial prior distribution is chosen for each of the F_j. This allows the joint prior distribution to be defined by

$$P(\hat{F}) = \prod_{j=0}^{m} \left[\frac{1}{F_j}\right]. \tag{13}$$

The joint posterior distribution is integrated numerically using the *evidence* procedure [29]. This also yields the marginal posterior distributions, i.e. the individual posterior distributions associated with each of the F_j. The values of each of the F_j at each iteration are saved in a histogram, known as the *trace*. At the same time, a posterior distribution for the total number of reactions is generated using Eqs. 9 & 10 and the values of each of the F_j at each iteration.

The true power of this MCMC-adapted TFractionFitter routine lies in the posterior distributions. If a particular F_j or N_R^{data} has a clear upper and lower bound, then the 0.16, 0.50, and 0.84 quantiles are reported as the low, median, and high value for the parameter. However, when analyzing data containing weak signals it is sometimes the case that no lower bound for the posterior distribution can be determined. In these cases the most accurate representation of the experimental result is an upper limit at the 0.95 quantile. Examples of both types of posterior distributions are given in Sec. IV C. This treatment gives a rigorous statistical definition of both upper limits and definitive values of branching ratios and total numbers of reactions. It should also be noted that if no upper limits are required during data analysis, then the results from the MCMC TFractionFitter method are nearly identical to those from the method described in Sec. III A.

C. Reference Resonance at $E_r^{c.m.} = 458$ keV

Absolute cross sections and resonance strengths were determined relative to the strength of the $E_r^{c.m.} = 458$ keV resonance. In general, the resonance strength can be expressed as (see Ref. [42])

$$\omega\gamma = \frac{2\epsilon_{eff}^{c.m.}}{\lambda_r^2}\frac{N_R^{data}}{N_B}, \tag{14}$$

where N_B is the total number of bombarding particles. All of the other parameters in the above equation refer to the 458-keV resonance and have been defined in Sec. II C. Using this relationship, the strength of any other resonance can be determined relative that of the 458-keV resonance by simply scaling the values of $\epsilon_{eff}^{c.m.}$, λ_r, N_R^{data}, and N_B associated with the measurement of that resonance. For a resonance at $E_{res} = E_r^{c.m.}$, we arrive at the equation [34, 42]

$$\omega\gamma(E_r^{c.m.}) = \omega\gamma(458\text{ keV})\left[\frac{\epsilon_{eff}^{E_{res}}}{\epsilon_{eff}^{458}}\right]\times\left[\frac{N_R^{E_{res}}}{N_R^{458}}\right] \times\left[\frac{\lambda_r^{458}}{\lambda_r^{E_{res}}}\right]^2\times\left[\frac{N_B^{458}}{N_B^{E_{res}}}\right], \tag{15}$$

where the notation has been compacted such that terms like $N_R^{data}(458\text{ keV})$ are represented as N_R^{458}.

This same procedure can be applied to direct-capture cross sections. If a DC measurement is made at a center-of-mass beam energy $E_{beam}^{c.m.} = E_o$ and an effective beam energy $E_{eff}^{c.m.} = E_o - \frac{1}{2}\Delta E = E_{DC}$, then the DC cross section at E_{DC} is given by

$$\sigma(E_{DC}) = \omega\gamma(458\text{ keV})\left[\frac{\epsilon_{eff}^{E_o}}{\epsilon_{eff}^{458}}\right]\times\left[\frac{N_R^{E_o}}{N_R^{458}}\right] \times\left[\frac{\left(\lambda_r^{458}\right)^2}{2\Delta E^{E_o}}\right]\times\left[\frac{N_B^{458}}{N_B^{E_o}}\right]. \tag{16}$$

This equation is essentially the same as Eq. 15 except that ΔE^{E_o} is used in place of the factor of $\lambda_r^2/2$. Note that Eq. 16 assumes an energy-independent cross section over the projectile energy as it loses energy within the target, as was the case for the targets yielding a total projectile energy loss of 6.5 keV employed for direct-capture measurements here.

The quantity N_B^{458} was obtained from a high-statistics measurement of the maximum yield from an unused target yielding a projectile energy loss of 21 keV at a laboratory-frame beam energy of $E_p^{lab} = 484$ keV and with an accumulated charge of 0.01 C of protons. Data were collected in both singles- and coincidence-detection modes. These data were analyzed using the method described in Sec. III A, but with one caveat. Instead of fitting the measured spectrum with individual templates for each primary decay from the resonant state, a single resonance template was created assuming the branching ratios of Ref. [30]. Since these branching ratios were obtained using the same analysis procedure employed here, there was no need to re-determine them. For consistency, we adopt the resonance strength of Ref. [30], $\omega\gamma(458\text{ keV}) = 0.583(43)$ eV.

The uncertainty budget for the results reported in this work is as follows. Each value of N_B in Eqs. 15 & 16 is assumed to have a 3% uncertainty [49]. A 4% uncertainty is assumed for $\epsilon_{eff}^{c.m.}(458\text{ keV})$ and $\epsilon_{eff}^{c.m.}(417\text{ keV})$ because there was no target degradation observed in those measurements. This uncertainty is estimated from variations seen in the relevant data included in the SRIM documentation [43]. Given the moderate amount of target degradation observed during the direct-capture measurements as well as during measurements of the 178-keV resonance, the uncertainty in $\epsilon_{eff}^{c.m.}(407\text{ keV})$ and $\epsilon_{eff}^{c.m.}(178\text{ keV})$ was increased to 9%, which included the uncertainty in the averaging procedure that was used to account for target degradation (as described in Sec. II C). In the case of the 151-keV resonance, the larger number of targets required for that measurement increased the uncertainty associated with target degradation, and thus $\epsilon_{eff}^{c.m.}(151\text{ keV})$ carried an uncertainty of 15%.

The uncertainty on N_R^{data} for each of the data sets varied depending on the quality of the fit to the observed spectra and ranged from 3% for $N_R^{data}(417\text{ keV})$ to 9% for $N_R^{data}(151\text{ keV})$. These uncertainties included an estimate of the systematic uncertainties in the GEANT templates, which is estimated from GEANT predictions of the total efficiency of the HPGe detector, as well as the uncertainty returned by the TFRACTIONFITTER class. Finally, all results included

the 7.3% uncertainty in $\omega\gamma$(458 keV) reported in Ref. [30] and a 3% uncertainty in N_R^{data}(458 keV), the latter of which was derived again included uncertainties related to the TFractionFitter and the statistics of the data set. Uncertainties on N_R^{data} values are considered statistical in nature while all other uncertainties are considered systematic.

IV. RESULTS

A. Resonance at $E_r^{c.m.}$ = 417 keV

A total of 0.03 C of data were collected on the 417-keV resonance at E_p^{lab} = 441 keV, yielding high-statistics spectra in both singles- and coincidence-detection modes. The coincidence spectrum had the additional condition that 3.5 MeV $\leq E_{NaI} + E_{HPGe} \leq$ 9.5 MeV. The lower limit was chosen to reduce environmental backgrounds whereas the upper limit was set just above the resonance excitation energy in order to reduce high-energy backgrounds. Both detection modes were analyzed according to the method described in Sec. III A by considering all potential L = 1 & 2 transitions from the resonant state, as opposed to only those transitions that were previously reported in Ref. [50] and Ref. [31]. The experimental singles spectrum is shown in Fig. 7 in black along with the fit to the data in green, the environmental room background in red, and selected resonance-decay templates shown in varying shades of blue. All resonance primary peaks are indicated with blue arrows.

As is apparent in Fig. 7, a number of primary transitions from this resonance were previously unidentified. These could be associated with the 417-keV resonance because they correspond to transitions to known excited states in ^{23}Na and follow the same excitation curve as transitions that have previously been associated with this resonance. For example, Fig. 8 shows excitation curves for the strong R→2982 γ ray and three previously unidentified transitions, R→5742, 7082, and 2076 keV (shown as the red diamonds, blue circles, and green squares, respectively). These three γ-ray transitions clearly follow the same energy trend as the R→2982 yield and are therefore associated with the 417-keV resonance in the ^{22}Ne(p,γ)^{23}Na reaction. Four additional new transitions were identified in a similar manner. Branching ratios for decays from this resonance, calculated using both singles- and coincidence-detection modes are listed in Table I alongside the previous results of Refs. [31, 50] for comparison. Recommended branching ratios calculated from the *unweighted* average of singles and coincidence values are shown in Table V alongside the recommended branching ratios for the other resonances measured for this work.

TABLE I: Branching ratios in % for primary transitions from the 417-keV resonance in the ^{22}Ne(p,γ)^{23}Na reaction measured here in singles- and coincidence-detection modes. The values of Refs. [31, 50] are shown for comparison.

Transition	Singles	Coincidence	Ref. [31]	Ref. [50]
R→0	3.75(24)	2.41(23)	1.2(6)	0.7
R→440	2.63(17)	3.16(22)	4.9(5)	2.1
R→2076	1.22(11)	1.32(13)	–	–
R→2391	1.34(12)	1.54(14)	2.9(3)	2.4
R→2640	3.00(20)	3.47(24)	6.4(5)	9.8
R→2982	26.6(15)	29.1(16)	22.4(10)	25
R→3678	1.05(16)	1.38(16)	3.1(4)	3.0
R→3848	2.46(18)	2.42(18)	2.0(3)	2.1
R→3914	22.1(12)	22.4(12)	30.0(17)	30
R→4430	2.96(20)	3.20(21)	4.7(4)	2.3
R→5742	1.75(15)	2.06(18)	–	–
R→5964	17.21(95)	16.62(93)	17.1(8)	17
R→6195	3.28(22)	2.20(17)	3.4(3)	3.3
R→6308	2.48(18)	2.07(16)	–	–
R→6868	2.12(17)	1.57(16)	–	–
R→6921	1.27(13)	1.21(14)	–	–
R→7082	2.98(21)	2.63(20)	–	–
R→7488	1.25(11)	0.90(9)	2.8(6)	2.3
R→7873	0.55(9)	0.34(9)	–	–

The strength of this resonance was determined according to Eq. 15 using both the singles and coincidence spectra

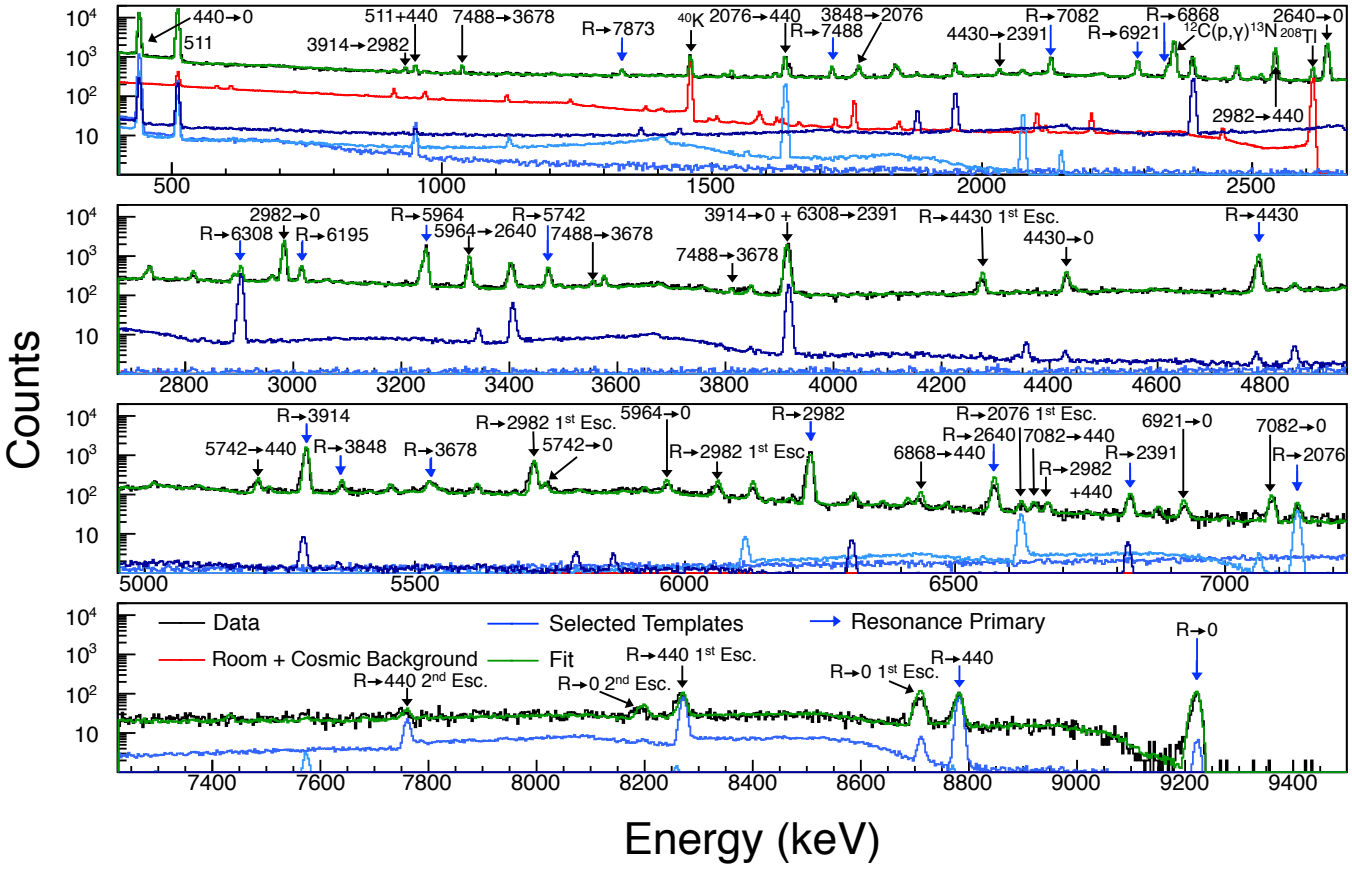

FIG. 7: (color online) The 417-keV resonance singles spectrum, from the the maximum yield of an unused, 21-keV thick ^{22}Ne target. The data are shown in black with the fit to the data shown in green. The fit was determined using the TFractionFitter [27] class of root [28] according to the method described in Sec. III A. The room-background and selected resonance-decay templates are shown in red and blue, respectively. Peaks corresponding to primary transitions are indicated with blue arrows. Although not every peak is labelled due to spatial constraints, each peak has been identified.

of the 417-keV resonance and an *unweighted* average of singles and coincidence results yields $\omega\gamma(417\text{ keV}) = 0.088(11)$ eV. As shown in Fig. 9, the strengths derived from the singles and coincidence are consistent with one another and agree well with previous results, once the latter are corrected as follows: The strength measured by Meyer *et al.* [50] was initially obtained relative to the strength of the 640-keV resonance in the ^{22}Ne$(p,\gamma)^{23}$Na reaction, reported in Ref. [51], but was subsequently renormalized by Endt [20] using the 1279-keV ^{22}Ne$(p,\gamma)^{23}$Na resonance strength reported in Ref. [52], yielding $\omega\gamma(417\text{ keV}) = 0.065(15)$. This is the strength that Depalo *et al.* [31] compared to their recommended strength, $\omega\gamma(417\text{ keV}) = 0.079(6)$ eV. However, the revision of the strength of the 458-keV resonance in Ref. [30] also changes the strength of the 1279-keV resonance. Given the new value of $\omega\gamma(458\text{ keV}) = 0.583(43)$ eV [30], $\omega\gamma(417\text{ keV})$ tabulated in Ref. [20] becomes 0.084(21) eV, and this is the value that we compare to in Fig. 9. It should be noted that Depalo *et al.* do not detect the new branches reported here, which amount to about 11% of the total decay strength. Adding this missing strength would imply $\omega\gamma(417\text{ keV}) = 0.088(7)$ eV. Nonetheless, there is excellent agreement between the present results, the revised strength from Meyer *et al.* [50] and the published value from Depalo *et al.* [31]. Consequently, we have taken a weighted average of the results of Refs. [50], [31], and the unweighted average of our singles and coincidence results. This yields a recommended $\omega\gamma(417\text{ keV}) = 0.082(5)$ eV.

A number of important points can be deduced from the results of this measurement. First and foremost for this work, the relative-measurement method described in Sec. III C appears to be successful as produces strengths that agree well with literature values. This validates the method of Sec. III C for use in subsequent sections. Second, excellent agreement is obtained between resonance strengths calculated with singles and coincidence data. This further verifies the accuracy of the GEANT simulation and characterization of the NaI annulus used in the analysis of

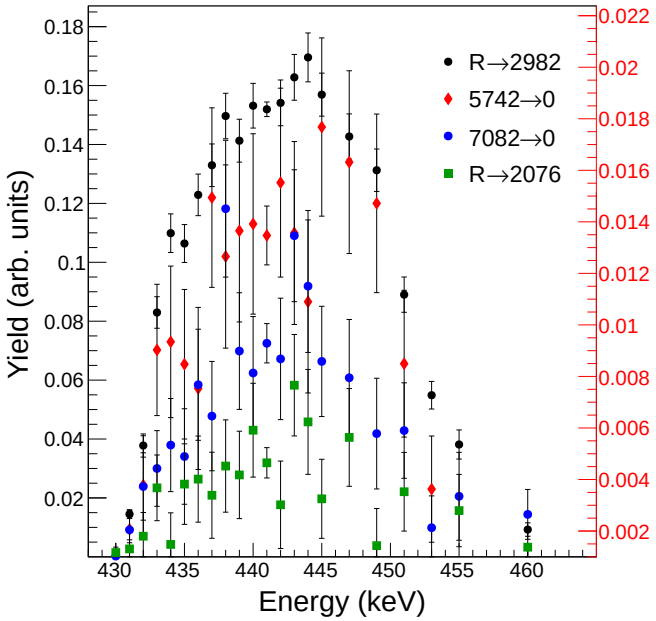

FIG. 8: (color online) A comparison of the target excitation curves obtained following the strong and previously known R→2982 decay primary γ ray, shown as black diamonds, to that of 3 γ rays corresponding to newly discovered transitions from the resonant state state to the 5742-, 7082-, and 2076-keV states, shown as red, blue, and green diamonds, circles, and squares, respectively. The yield scale for the R→2982 transition excitation curve is shown on the left and the scale for all other γ rays shown here is on the right. The existence of these resonant state transitions is verified by the excitation curve similarity between the new γ rays and the R→2982 transition. In addition, four more transitions were identified, the γ rays for which follow a similar trend to that of the γ rays shown here

coincidence data. Finally, the analysis of data using the method described in Sec. III A has shown once again that it has the potential to facilitate the identification of new branching ratios that are otherwise difficult to identify in a traditional peak-by-peak analysis.

B. Direct Capture Measurement at 425 keV

Within the Gamow window corresponding to the massive AGB star modeled in Ref. [16], there is competition between the direct-capture process and resonance capture. The non-resonant cross section formalism can be found in numerous textbooks [42] is not repeated here. The direct-capture cross section, σ_{DC}, measurements of Görres *et al.* [53] are consistent with $S(E) = 62$ keV b = constant, which has been used as input in subsequent reaction-rate compilations. Their measurements covered the energy range E_p^{lab} ∼550 keV – 1600 keV and were extrapolated to lower energies using a DC model that was normalized to the experimental data. We have extended this measurement to an energy $E_p^{lab} = 425$ keV ($E_p^{c.m.} = 407$ keV, corresponding to an expected decrease in cross section of a factor of 5). This energy was chosen to ensure that significant statistics would be acquired while also avoiding the strong ^{22}Ne(p,γ)^{23}Na resonances at $E_r^{c.m.} = 458$ and 417 keV.

A total of 5 C of data were collected on targets with $\Delta E \approx 6.5$ keV. All results quoted here were obtained from coincidence data with an energy gate of 4.5 MeV $\leq E_{NaI} + E_{HPGe} \leq 9.5$ MeV, using the method described in Sec. III A. Note that the lower limit of 4.5 MeV is higher than that used for the 417-keV resonance, and was chosen to yield the best signal-to-background ratio for $E_\gamma \leq 4.5$ MeV. Transitions to the 440-, 2391-, 2982-, and 6308-keV states in ^{23}Na were extracted and are compared in Fig. 10 to existing data from Refs. [53–55], as well as the DC-model fit from Ref. [53]. In general, agreement is obtained between the present data points and the DC-model expectation for the transitions shown in Fig. 10. A similar level of agreement was obtained for DC transitions to the 6921-, 7082-, 7488-, 8664-, and 8830-keV states. The cross sections measured in this work are recorded in Table II.

A number of γ-ray peaks were observed that could not be associated with known transitions. In fact, Ref. [53] quotes upper limits for contributions to the direct-capture strength from the DC→8862, 8894, 8945, 8972, and 9000

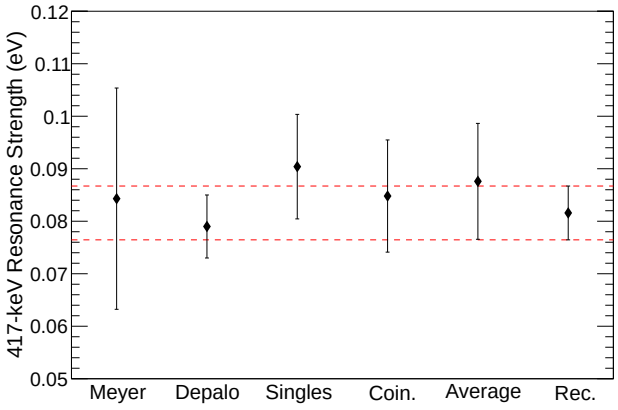

FIG. 9: A comparison of the literature $\omega\gamma$(417 keV) values from [50] and [31] to the presently measured singles and coincidence values. The [50] result has been scaled according the increase in $\omega\gamma$(458 keV) reported in [30]. The recommended value is calculated from a weighted average of the results of the two literature strengths and the *unweighted* average of the strengths deduced from singles and coincidence results shown here.

TABLE II: A summary of the measured direct-capture cross sections for the ^{22}Ne(p,γ)^{23}Na reaction. All cross sections and uncertainties are reported in units of nb.

Transition	σ_{DC}(407 keV)	$\delta\sigma_{DC,stat}$	$\delta\sigma_{DC,sys}$
DC→0	16.4(26)	1.1	2.1
DC→440	6.1(14)	1.1	0.8
DC→2391	9.9(17)	1.0	1.3
DC→2982	3.8(10)	0.9	0.5
DC→6308	3.1(9)	0.8	0.4
DC→6921	0.8(6)	0.6	0.1
DC→7082	1.6(7)	0.7	0.2
DC→7488	1.1(7)	0.7	0.1
DC→8664	8.0(14)	0.9	1.0
DC→8830	1.9(14)	1.4	0.2

transitions. These were not included in our analysis because no literature data exist on the decays from these states. Thus no decay templates could be constructed. However, these transitions make a negligible contribution to the total DC cross section. The DC→0 transition was easily observed, but exhibits an interesting and presently unexplained energy dependence [53, 55], which complicates the extrapolation to lower energies. The present and previous results for σ_{DC} are shown in the top panel of Fig. 11 and the corresponding S-factor is displayed in the bottom panel. The authors of Ref. [53] speculated that the trend of increasing average S-factor in the bottom panel of Fig. 11 may be explained by an interference between the DC process and the resonances at E_r^{lab} = 35 and -129 keV. However, the γ-ray angular distribution is asymmetric about 90^o angle and this asymmetry changes sign with beam energy, which is not consistent with a simple DC-resonance interference.

It was pointed out in Ref. [53] that this kind of complicated energy dependence of cross section and angular distribution could be explained by a phenomenon known as Ericson fluctuations [56] in which strongly-overlapping levels produce an anomalous energy dependence in the nuclear cross section. If this is the case, then similar fluctuations would be expected from other DC transitions, but are not observed.

Regardless of the actual source of the of the fluctuations observed in the DC→0 transition, it is clear that the DC model from Ref. [53] underestimates the observed partial cross section. An effort to obtain a better estimate of the of the average S-factor is performed in Ref. [39] using an effective S-factor [42]. These fits to the data are shown in the bottom panel of Fig. 11 as the dashed lines. The blue and black dished lines are effective S-factor fits to the data of Refs. [53] and [54], respectively, as well as to the present data point. It was concluded in Ref. [39] that the direct-capture ^{22}Ne(p,γ)^{23}Na reaction rate appears to be unimportant from the standpoint of thermally pulsing AGB

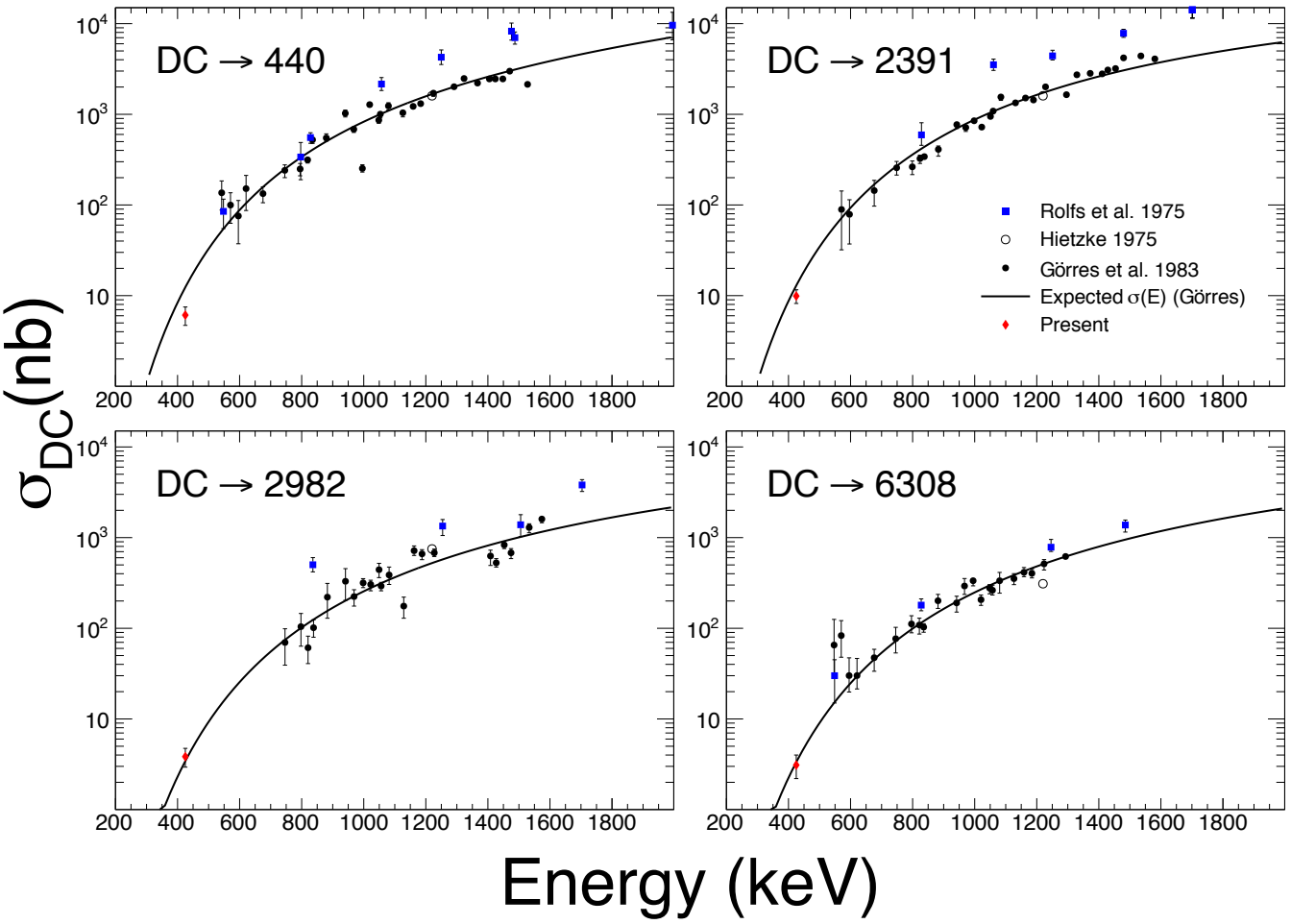

FIG. 10: (color online) A comparison of the measured partial direct-capture cross sections at E_p^{lab} = 425 keV to the literature direct-capture cross sections for the DC→440, 2391, 2982, & 6308 transitions. The results of Refs. [54], [53], the ∼1.2 MeV data point of Ref. [55], and the present data points are shown as the blue squares, black circles, open circles, and red diamonds, respectively. The DC-model prediction calculated by Ref. [53] is shown as the solid black line.

stars and the Na-O anti-correlation in globular clusters. This point will be further discussed in Sec. V.

C. Resonance at $E_r^{c.m.}$ = 178 keV

The $E_r^{c.m.}$ = 178 keV resonance was measured at a beam energy of E_p^{lab} = 192 keV. A total beam charge of 30 C was deposited on three ^{22}Ne targets and target degradation was accounted for using the method described in Sec. II C. A trapezoidal coincidence gate of 2.8 MeV $\leq E_{NaI} + E_{HPGe} \leq$ 9.5 MeV was chosen, and although the lower coincidence limit was low enough to allow some ^{208}Tl γ rays into the coincidence spectrum, this gate provided the best signal/background for low-energy transitions. A significant signal from this resonance was observed both in singles and coincidence. The 440-keV γ ray, corresponding to the 440→0 transition, is shown in Fig. 12a. Singles and coincidence data are shown in blue in the top and bottom panels, respectively. Also, 60 C of off-resonance data just below the 151-keV resonance were collected. The off-resonance data were scaled to match the total beam charge collected on this resonance and are shown in red for comparison.

The coincidence spectrum obtained on this resonance is shown in Fig. 13 with the data spectrum, the room-background, and selected resonance-decay templates, and the fit to the data shown in black, red, blue, and green, respectively. Primary peaks are indicated by the blue arrows. Note that no ground-state transition peak is observed

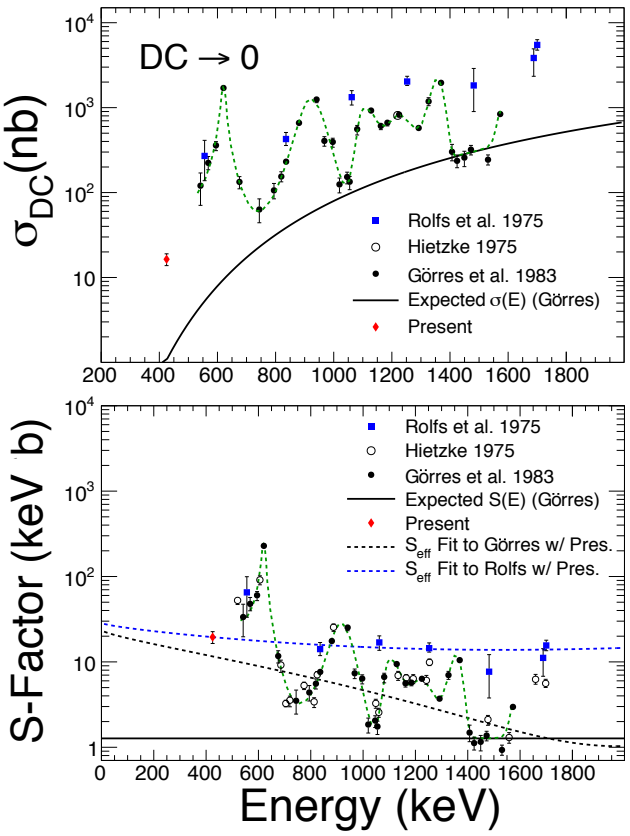

FIG. 11: (color online) Comparison of the measured DC→0 transition partial σ_{DC} (top panel) and partial S-factor (bottom panel), shown as red diamonds, to the literature values from Refs. [54], [55], and [53], shown as blue squares, open circles, and black circles, respectively. The expected σ_{DC} and S-factor trend from the DC-model prediction of Ref. [53] are shown as the solid black line in the top and bottom panels and the effective S-factor fits to the data from Refs. [53] and [54] are shown as the black and blue dashed lines. The green dashed lines in both the top and bottom panels are to guide the eye. See the text for a discussion of these data.

in coincidence because if the full ground-state γ-ray energy is observed, then there are no other secondary γ rays available for coincidence detection. However, the escape peaks and Compton-scattered γ rays of the ground-state γ ray can be seen. The fit to this data set was not extended below the 511-keV peak because the signal from this resonance was fairly strong. Therefore, the well-defined features present in the data spectrum above the 511-keV peak were sufficient to provide an accurate fit to the data and the additional constraint of the 440-keV peak was not necessary. This claim is supported by the fact the calculated branching ratios and partial numbers of reactions derived for each primary transition yielded a total number of expected counts in the 440-keV peak that is in agreement with that observed.

Because a number of apparent decay branches were too weak to be definitively identified, we made use of the MCMC-adapted TFractionFitter routine described in Sec. III B. The branching ratios derived from the singles and coincidence data are shown in Table III. Unfortunately, it is difficult to compare these branching ratios with previous work. The spectrum shown in Ref. [26] indicates many of the same transitions that are listed in Table III, but no branching ratios were reported. Jenkins *et al.* [21] observed only the transition to the 2982-keV state, which we confirm. However, because they could not isolate transitions from specific states, we can not extract a branching ratio from their measurement. Our recommended branching ratios were derived in the following manner: In cases where there was at least one definitive measurement of a particular branch, the recommended branching ratio was derived by averaging the 0.50 quantiles of the marginal posterior distribution from both data sets and the uncertainties on the recommended branching ratios were determined by averaging the percent differences between the 0.50 and 0.68 quantiles of both posterior distributions. However, if both singles and coincidence measurements resulted in an upper limit, then the lower of the two upper limits was recommended. The recommended branching ratios from this resonance calculated in the manner described here are summarized in Table V.

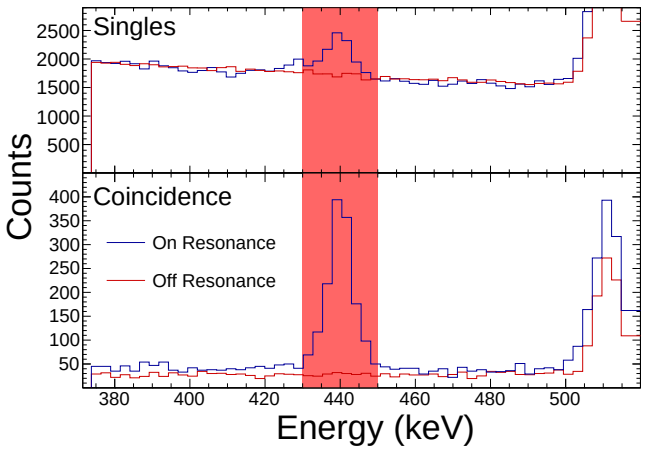

(a) The 440→0 transition from the decay of the 178-keV resonance in both singles and coincidence modes.

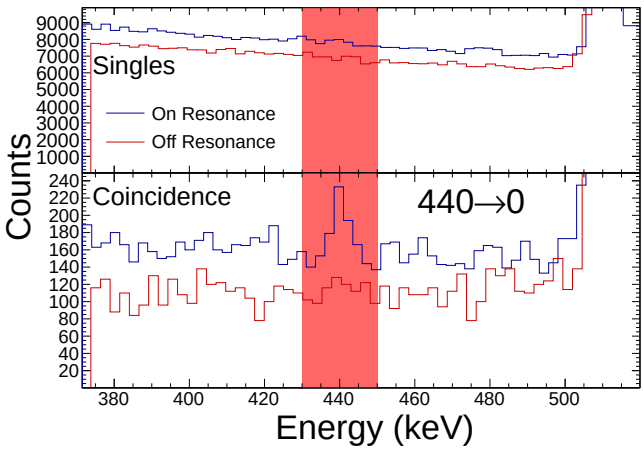

(b) The 440→0 transition from the decay of the 151-keV resonance in both singles and coincidence modes.

FIG. 12: (color online) A comparison of the 440-keV γ-ray signal obtained from the 178- and 151-keV resonances in the ^{22}Ne(p,γ)^{23}Na reaction are shown in blue on the left- and right-hand plots, respectively. In each plot singles data are shown on the top panel and coincidence data are shown on the bottom. Off-resonance data are shown in red on each plot as well. In both cases the off-resonance data shown was scaled to match the total beam charge collected on either resonance.

TABLE III: Branching ratios in % for primary transitions from the 178-keV resonance in the ^{22}Ne(p,γ)^{23}Na reaction derived using the MCMC TFractionFitter routine described in Ref. [29].

Transition	Singles	Coincidence
R→0	7.9(13)	≤6.1
R→440	34.7(13)	40.7(19)
R→2076	38.7(13)	41.0(13)
R→2982	5.2(8)	4.9(8)
R→3678	3.2(8)	≤2.6
R→3914	3.2(6)	3.1(7)
R→4775	≤3.0	≤3.4
R→6618	5.4(10)	4.0(8)

Examples of the marginal posterior distribution and the trace associated with the coincidence measurement of the R→2982 and R→0 transitions are shown in the top and bottom panels of Figs. 14a & 14b, respectively. These figures provide excellent examples of the a definitive detection (the coincidence R→2982 transition) and a detection requiring an upper limit (the coincidence R→0 transition). The measurement of the coincidence R→2982 transition in Fig. 14a shows a clear posterior distribution that is well above zero and corresponds to the branch quoted in Table III. On the other hand, the coincidence R→0 posterior distribution in Fig. 14b is consistent with no detection and lends itself to an upper limit determined according to the 0.95 quantile of the corresponding marginal posterior distribution.

Observations of this resonance reveal two important points. First, a ground-state transition is definitively observed in singles mode, an upper limit for a ground-state transition was determined from the coincidence data, and the 6618-, 3914-, 2982-, and 2076-keV states were observed to be populated during these measurements. Each of these states has a non-zero transition probability to the ground state. This means that a significant portion of the observed strength bypasses both the 2076- and 440-keV states in ^{23}Na. Therefore, the assumption of a 100% branch to the 440-keV state made in Refs. [57] & [24] is incorrect. Second, the spin and parity of the 8972-keV resonant state has been restricted to $J^\pi(8972\text{ keV}) = 3/2^+, 5/2^+$ [23]. However, over 75% of the observed decay strength in both singles and coincidence is observed to go directly to the 440- and 2076-keV states which have $J^\pi(440\text{ keV}) = 5/2^+$ and $J^\pi(2076\text{ keV}) = 7/2^+$. This evidence combined with the considerably lower observed ground-state-transition strength ($J^\pi(0\text{ keV}) = 3/2^+$) indicate that the resonant state is likely $J^\pi(8972\text{ keV}) = 5/2^+$. This spin-parity assignment agrees with the assessment of Ref. [21], which was determined based on γ-γ measurements of the ^{12}C(^{12}C,p)^{23}Na reaction

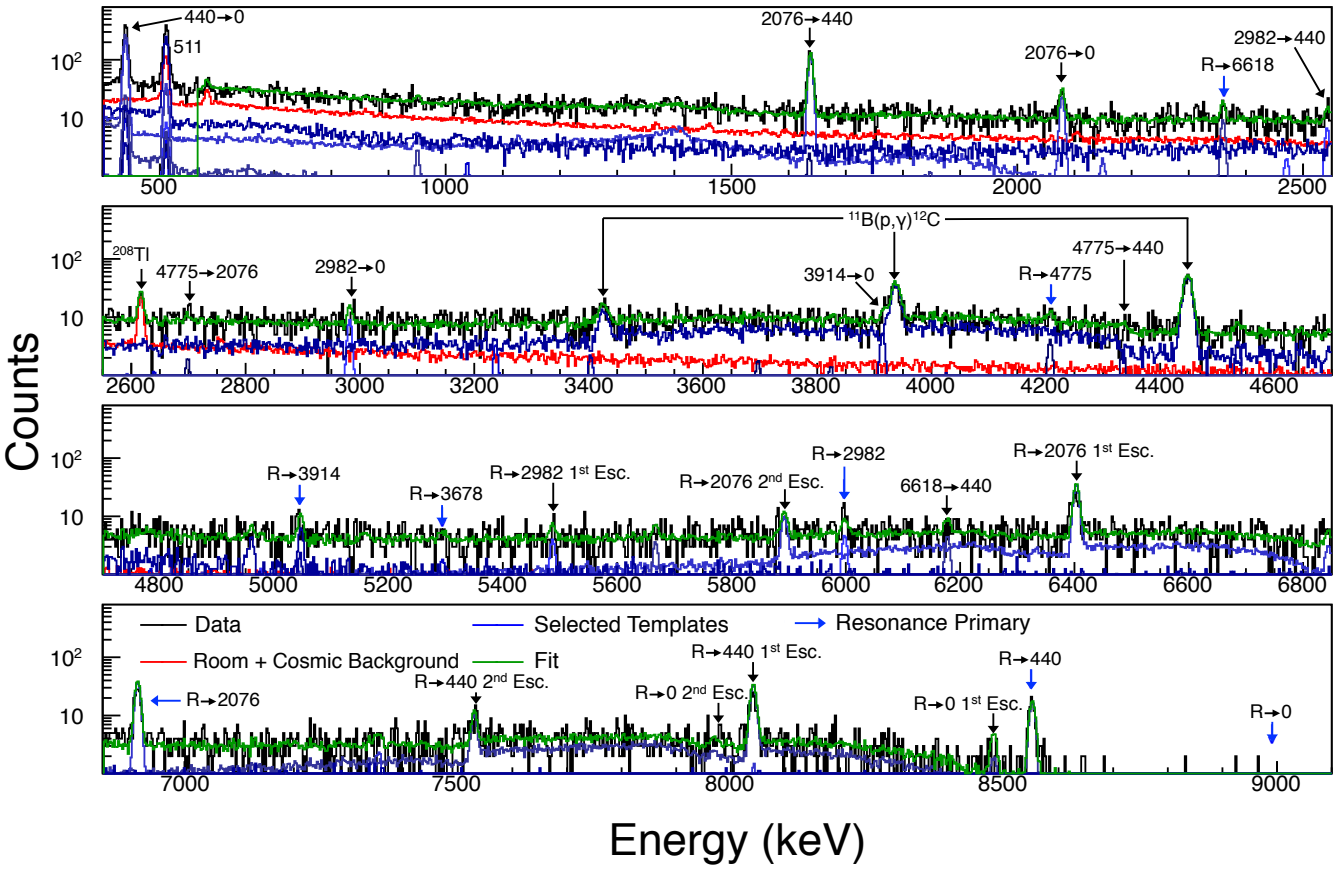

FIG. 13: (color online) The coincidence spectrum of the 178-keV resonance in the ^{22}Ne(p,γ)^{23}Na reaction measured with 30 C of beam on target. The data are shown black with the room-background and selected resonance-decay templates shown in red and blue, respectively. The fit to the data is shown in green with all resonance primary peaks indicated by the blue arrows. Note that no ground-state-transition primary peak is seen here because of the coincidence requirement. However, evidence for its escape peaks can be seen.

and is in contrast to the value of $J^{\pi}(8972\text{ keV}) = 1/2^{+}$ assumed in Ref. [22]. Thus, we have adopted $J^{\pi} = 5/2^{+}$ for this resonance.

The total number of reactions, N_R^{data}, for both singles- and coincidence-detection modes is described by a posterior distribution that is consistent with a definitive detection of this resonance. We recommend a resonance strength of $\omega\gamma(178\text{ keV}) = 2.32(32)\times10^{-6}$ eV based on an *unweighted* average of the strengths calculated using both detection modes. This value is consistent with both the resonance strength lower limit of $\omega\gamma(178\text{ keV}) \geq 1.2\times10^{-7}$ eV set by Ref. [24] and the upper limit of $\omega\gamma(178\text{ keV}) \leq 2.6\times10^{-6}$ eV reported in Ref. [57]. However, our value is just outside of agreement at the 1-σ level with the value of $\omega\gamma(178\text{ keV}) = 1.87(6)\times10^{-6}$ eV reported in Refs. [26, 58]. However, there are no branching ratios to the 3678-keV or ground states reported in Ref. [58]. If this missing strength were included, then the strength of Refs. [26, 58] would be very close to if not in agreement with the present result. As will be shown in Secs. V & VI, the identification of a definitive strength for this resonance has a profound impact on the total ^{22}Ne(p,γ)^{23}Na reaction rate and on the nucleosynthesis that occurs in thermally pulsing AGB stars.

D. Resonance at $E_r^{c.m.} = 151$ keV

A total of 120 C of data were collected on the 151-keV resonance using a proton energy of $E_p^{lab} = 165$ keV. Note that this beam energy is nearly on the maximum of the strong, broad resonance in the ^{11}B(p,γ)^{12}C reaction. This beam-induced contaminant was a significant issue during data analysis. In order to minimize this background, a coincidence

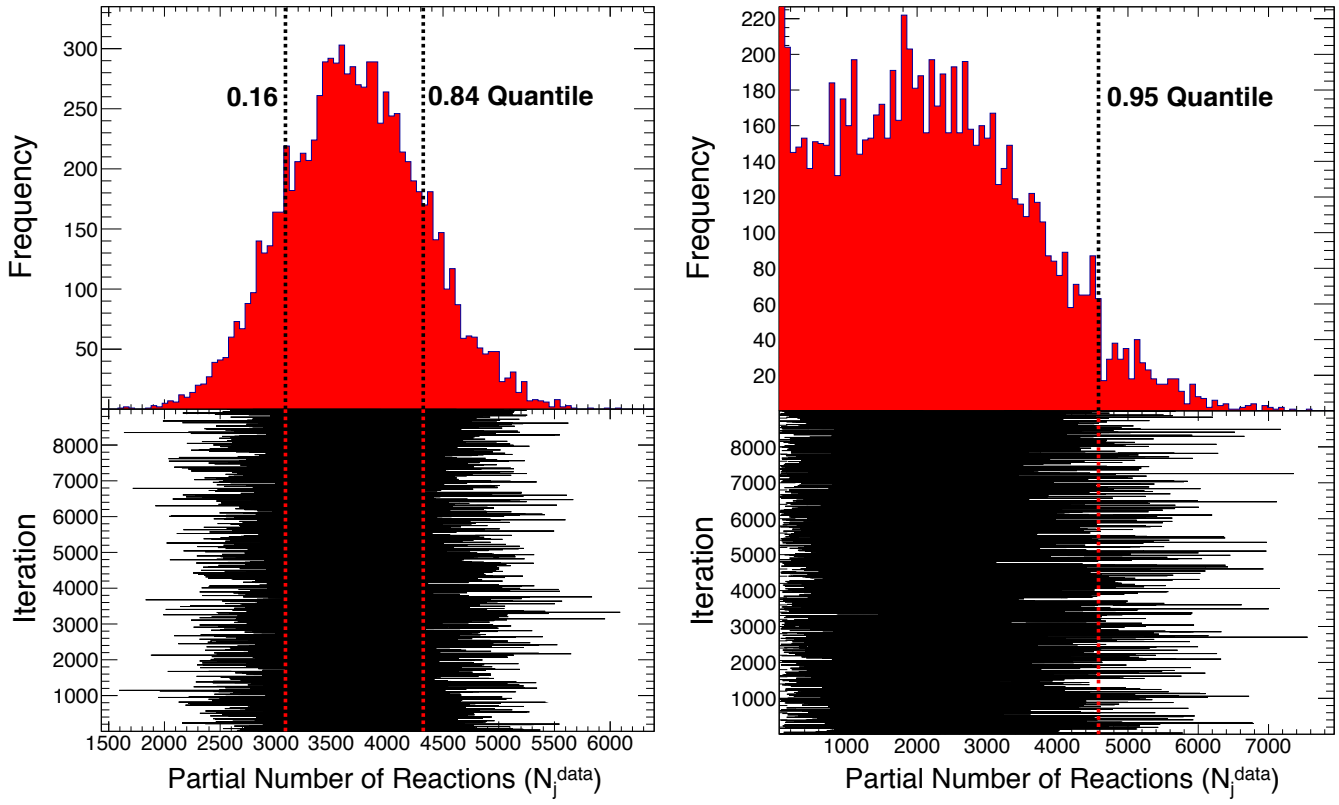

(a) Posterior distribution of the coincidence R→2982 transition from the 178-keV resonance.

(b) Posterior distribution of the coincidence R→0 transition from the 178-keV resonance.

FIG. 14: (color online) The top and bottom panels show the marginal posterior distribution and the trace corresponding to the coincidence R→2982 transition measurement from this resonance. This transition provides an excellent example of a well-defined posterior distribution corresponding to a definitive detection of the this transition. The partial number of reactions for this particular resonance decay is given by the 0.50 quantile of the posterior distribution while the uncertainties are derived from the 0.16 and 0.84 quantiles for a 68% coverage probability.

gate was drawn specifically to avoid known γ rays from this reaction. This gate provided a higher signal-to-background ratio than the typical trapezoidal gate in the γ-ray peaks of interest.

It was expected that there would be a strong overall branch to the 440-keV state from this resonance. Indeed a signal at 440 keV was observed in the coincidence spectrum from this resonance. This 440-keV region is shown in Fig. 12b using singles- and coincidence-detection modes (top and bottom panel, respectively) with off-resonance coincidence data shown in red for comparison. The 60 C of off-resonance data was scaled to match the total beam charge taken on resonance. Note that while there is no significant signal in the singles spectrum at 440-keV, the background in this region drops by near a factor of 100 in coincidence detection mode, revealing the 440-keV peak. All results for this resonance were determined using coincidence data and the analysis method described in Sec. III B.

A strong primary transition was to the 3914-keV state was observed in this data set. The singles and coincidence signals for this transition are shown in the upper left panel of Fig. 15. Three other regions of the spectrum believed to contain signals from this resonance are shown in the remaining panels of Fig. 15. The R→3914 transition is especially interesting because over 80% of the decays from the 3914-keV state go to states other than the 440-keV state. Therefore, this transition represents a strong contribution to the observed strength that would be completely missed if one were to assume a 100% overall branch to the 440-keV state. Unfortunately, the 3914→0 secondary peak is overshadowed by the 3929-keV first-escape peak from of 4.44 MeV ^{11}B(p,γ)^{12}C secondary γ ray present in our data spectrum.

The upper and lower right panels of Fig. 15 show evidence suggesting that the 2391-keV state was also populated by this resonance. Given that the 3914-keV state decays to the 2391-keV state with a ∼1% branch (see Ref. [23]), it is more likely that this state was populated via a primary transition from the resonant state. Finally, there appears

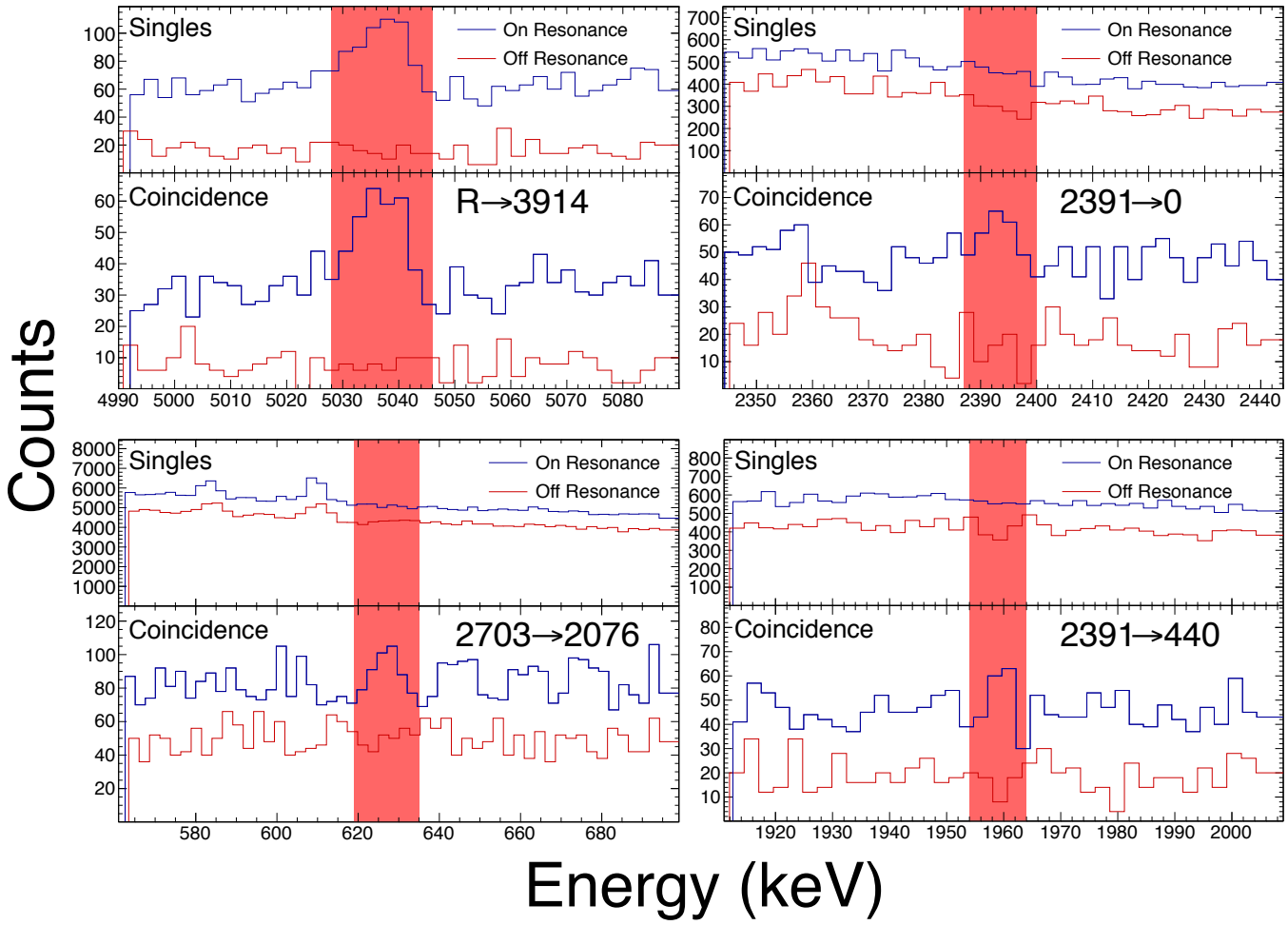

FIG. 15: (color online) The singles (top panel) and coincidence (bottom panel) signals from the R→3914 transition observed during measurements of the 151-keV resonance in the ^{22}Ne(p,γ)^{23}Na reaction. Coincidence off-resonance data are shown on the bottom panel for comparison. The observation of this primary γ ray indicates a significant portion of the observed strength that completely bypasses the 440-keV state.

to be a weak signal observed at 627 keV possibly corresponding to a transition from the 2703-keV state in ^{23}Na to the 2076-keV state, shown in the lower left panel of Fig. 15. We see no clear evidence for the R→2703 keV transition, which clearly disagrees with the tabulated [20] branching ratio of 100%.

This erroneous branching ratio has contributed to confusion in the literature concerning the J^π for this resonance, which impacts earlier estimates of the resonance strength as well as our interpretation of the γ-ray spectrum shown in Fig. 17. Thus, some clarification is in order. It was previously assumed that this resonance corresponds to a single excited state in ^{23}Na at E$_x$ = 8945 keV. This single state was believed to possess $J^\pi = 5/2^-$, $7/2^-$ in Ref. [23]. Although the $5/2^-$ and $7/2^-$ assignments are said to originate from ^{22}Ne(^{3}He,d)^{23}Na measurements by Ref. [59] and ^{22}Ne(d,n)^{23}Na by Ref. [60], respectively, it should be noted that the $5/2^-$ assignment in Ref. [23] may actually be based on a misprint in Ref. [59]. The authors of Ref. [19] estimated the strength of this resonance via ^{22}Ne(^{3}He,d)^{23}Na, with the assumption of L = 3 transfer and $J^\pi = 7/2^-$. The latter was based on the tabulated [20] 100% branch to the $9/2^+$ 2703-keV state. This choice significantly impacted the deduced strength and will be discussed in more detail at the end of this section.

More recently, Ref. [21] studied states in ^{23}Na via the ^{12}C(^{12}C,$p\gamma$)^{23}Na reaction and discovered that this resonance may actually be a doublet of states with one member having $J^\pi = 7/2^-$ while the other was tentatively assigned $3/2^+$. It follows that the $3/2^+$ resonance should be the more easily populated of the two states, but this is contrary to the reported results in the literature. However, a re-analysis of the data reported in Ref. [19], shown in Fig. 16, indicates

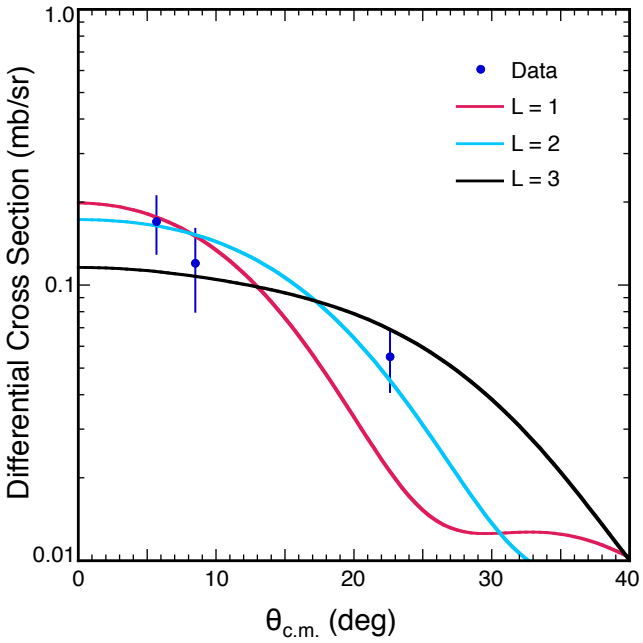

FIG. 16: (color online) Fits to the ^{22}Ne(^{3}He,d)^{23}Na data from Ref. [19] corresponding to the 8945-keV state in ^{23}Na assuming L = 1, 2, & 3 angular momentum transfer. Figure courtesy of A. E. Champagne. See text for a discussion.

that the observed angular distribution of the emitted deuterons is also consistent with L = 2 angular momentum transfer, which would be consistent with $J^{\pi} = 3/2^{+}$ and would also significantly increase the deduced strength.

Jenkins *et al.* [21] report primary branches from the $3/2^{+}$ resonant state to the $5/2^{+}$ 3914-keV state and to the $1/2^{+}$ 2391-keV state of ^{23}Na. Although neither of these are E1 transitions, nearby states of the same spin and parity (e.g., the 9211-keV state) tend to naturally undergo more M1 transitions than E1. As was mentioned earlier, evidence for both of these transitions was observed in our data. Additionally, they reported primary branches from the $7/2^{-}$ state to the 7125-, 6353-, 2703-, and 2076-keV states. The only evidence for this higher-spin resonance observed in this work is the potential decay from the 2703-keV state in ^{23}Na shown in Fig. 15 because this state is not populated by either observed decay from the $3/2^{+}$ resonance state.

Templates for both transitions from the $3/2^{+}$ states associated with this resonance were included in the fit to these data because signals associated with those transitions were clearly observed. Additionally, there is tentative evidence that the 2703-keV state was populated during data acquisition, but this population could be the result of a primary decay to the 2703-keV state or a secondary decay from the 7125- or 6353-keV states. Therefore, templates for all three of these transitions observed in Ref. [21] were included in the fit to these data. Finally, the R→2076 transition template was included for consistency with Ref. [21]. Branching ratios from Ref. [21] were employed for secondary decays from the 6353- and 7125-keV states because the branches from those states were measured to be significantly different than those reported in Ref. [23].

Relative branching ratios for R→2391 and 3914 transitions from the $3/2^{+}$ state are shown in Table IV compared to those reported in Jenkins *et al.* [21]. The present branching ratios agree with those of the recently-published publication by the LUNA collaboration as well [58]. We recommend a strength of $\omega\gamma(151\text{ keV}; 3/2^{+}) = 2.03(40)\times10^{-7}$ eV for this state in the doublet proposed by Ref. [21]. While in principle branching ratios for the transitions included corresponding to the $7/2^{-}$ resonant state could be derived from the relative partial numbers of reactions, little evidence exists for these transitions beyond the tentative 2703→2076-keV transition discussed above. Therefore, no branches for these transitions were determined and an upper limit of $\omega\gamma(151\text{ keV}; 7/2^{-}) \leq 9.7\times10^{-8}$ eV is recommended based on the 0.95 quantile of the posterior distribution corresponding to the sum of all transitions from the $7/2^{-}$ resonant state.

The $\omega\gamma(151\text{ keV}; 3/2^{+})$ value reported here is higher than and just outside of agreement at the 1-σ level with the result of Refs. [26, 58], $\omega\gamma(151\text{ keV}) = 1.48(10)\text{ x }10^{-7}$ eV. While the branching ratios from $3/2^{+}$ resonance at 151 keV reported in Ref. [58] agree with those reported here, the present results utilize the Compton background as well as the peaks of interest and there is no background subtraction to consider in the method employed in this work.

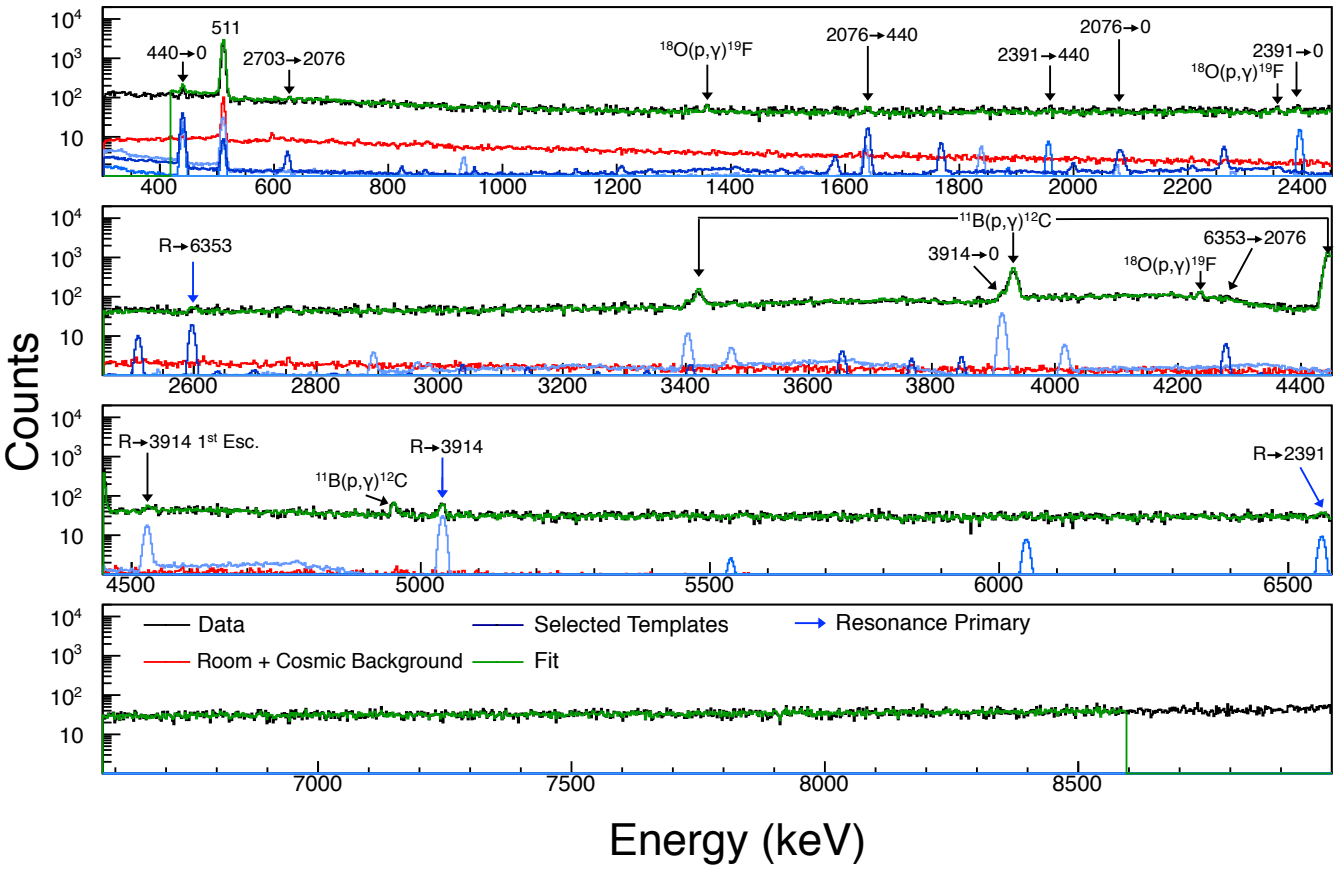

FIG. 17: (color online) The coincidence spectrum obtained from a total of 120 C of data collected on target on the 151-keV resonance in the ^{22}Ne(p,γ)^{23}Na reaction. The data are shown in black. Templates for the room background and selected resonance decays are shown in red and blue, respectively, and the fit to the data is shown in green. Blue arrows indicate the position of the resonance primary peaks associated with the transitions used for the fit to the data. Note that templates for the R→2076, 2703, 6353, and 7125 transitions were included to account for the weak peak observed at 627 keV and also for consistency with the branches reported in Ref. [21].

These advantages in data analysis may have allowed for a more reliable estimate of the total number of counts.

A separate comparison of the present results to those of recent ^{22}Ne(^{3}He,d)^{23}Na measurements is in order as well. Hale *et al.* [19] reported a strength of $\omega\gamma$(151 keV) $\leq 9.2\times10^{-9}$ eV while the authors of Ref. [22] adopted $\omega\gamma$(151 keV) $= 9.2\times10^{-9}$ eV based on the recommendation of Ref. [18]. This strength was calculated from the spectroscopic factor for the 8945-keV state, assuming L = 3 transfer, consistent with $J^\pi = 7/2^-$. Given the quality of their angular distribution (reproduced in Fig.16), an L = 2 fit was only ruled out based on this assumed J^π. However, with $J^\pi = 3/2^+$, the L = 2 fit implies $\omega\gamma$(151 keV) $= 3.0\times10^{-7}$ eV, which is a factor of ∼30 higher than the value adopted in Ref. [22] and in much better agreement with the strengths reported here and in Ref. [26].

TABLE IV: Branching ratios for primary transitions from the $3/2^+$ 8945-keV state corresponding to one state of the doublet proposed to comprise 151-keV resonance in the ^{22}Ne(p,γ)^{23}Na reaction. No branching ratios are reported here for the $7/2^-$ resonance because of the lack of observational evidence for these decays.

	Branching Ratio (%)	
Transition	Present	Ref. [21]
R→2391	20(4)	39(6)
R→3914	80(6)	61(30)

V. THERMONUCLEAR REACTION RATE OF ^{22}Ne(p,γ)^{23}Na

In this paper we report on new measurements of resonance strengths for the 151-keV ($3/2^+$), 178-keV, and 417-keV resonances in the ^{22}Ne(p,γ)^{23}Na reaction. Recommended branching ratios for the decay of these resonances are listed in TableV. We have also measured the direct-capture cross section at $E_p^{c.m.} = 407$ keV and an upper limit for the potential $7/2^-$ resonance at 151 keV. Resonance strengths are summarized in Table VI. The DC cross sections are shown in Table II and are not repeated here. Given these results, we may also calculate a new thermonuclear reaction rate for the ^{22}Ne(p,γ)^{23}Na reaction.

TABLE V: Recommended branching ratios in % for primary transitions from the 417-, 178-, and 151-keV resonances in the ^{22}Ne(p,γ)^{23}Na reaction. Note that the branching ratios from the 151-keV resonance only correspond to the $3/2^+$ state in the doublet proposed in Ref. [21].

	γ decay in % from Resonances at $E_r^{c.m.}$		
Transition	417	178	151
R→0	3.08(23)	5.3(14)	–
R→440	2.89(19)	37.7(15)	–
R→2076	1.27(12)	39.8(13)	–
R→2391	1.44(13)	–	20(4)
R→2640	3.23(22)	–	–
R→2982	27.8(15)	5.0(8)	–
R→3678	1.21(16)	2.2(8)	–
R→3848	2.44(18)	–	–
R→3914	22.2(12)	3.1(6)	80(6)
R→4430	3.08(20)	–	–
R→4775	–	≤3.0	–
R→5742	1.90(16)	–	–
R→5964	16.9(94)	–	–
R→6195	2.74(19)	–	–
R→6308	2.27(17)	–	–
R→6618	–	4.7(9)	–
R→6868	1.84(17)	–	–
R→6921	1.24(13)	–	–
R→7082	2.80(20)	–	–
R→7488	1.07(10)	–	–
R→7873	0.44(9)	–	–

TABLE VI: A summary of the measured resonance strengths for the ^{22}Ne(p,γ)^{23}Na reaction and a comparison to literature values. All strengths are reported in units of eV. Note that the stronger of the two states involved doublet at 151 keV is assumed to have $J^\pi = 3/2^+$ as opposed to $J^\pi = 7/2^-$ in accordance with the spin assignment of Ref. [21] and the re-analysis of transfer-reaction data from Ref. [19]. See the text associated with each strength for detailed descriptions.

	Present	Cavanna *et al.* (2015)	Depalo *et al.* (2015)	Recommended
$\omega\gamma$(417 keV)	$(8.8\pm0.5_{stat}\pm0.9_{sys})\times10^{-2}$	–	$(7.9\pm0.2_{stat}\pm0.8_{sys})\times10^{-2}$	$8.2(5)\times10^{-2}$
$\omega\gamma$(178 keV)	$(2.32\pm0.12_{stat}\pm0.30_{sys})\times10^{-6}$	$1.87(6)\times10^{-6}$	–	$2.32(32)\times10^{-6}$
$\omega\gamma$(151 keV; $3/2^+$)	$(2.03\pm0.18_{stat}\pm0.35_{sys})\times10^{-7}$	$1.48(10)\times10^{-7}$	–	$2.03(40)\times10^{-7}$
$\omega\gamma$(151 keV; $7/2^-$)	$\leq 9.7\times10^{-8}$	–	–	$\leq 9.7\times10^{-8}$

Given that there are no interfering resonances to consider in the ^{22}Ne(p,γ)^{23}Na reaction, the total resonant rate is a simple sum of all narrow resonances and the total reaction rate is the sum of the total resonant and direct-

capture reaction rates [42]. A numerical table of the thermonuclear reaction rate for the ^{22}Ne(p,γ)^{23}Na reaction was calculated with the code RATESMC and is given in Table VII. The input to RATESMC included the present results and the revised strength for the 458-keV resonance [30]. The latter value was used to the correct the strengths of higher-lying resonances where appropriate. As we discussed in Sec. IV B, a constant S-factor of 62 keV b from Ref. [53] was previously adopted in the STARLIB reaction rate library. It is this S-factor that was employed in the RATESMC calculation. Given our finding (Ref. [39] and the present work) that the DC rate of the ^{22}Ne(p,γ)^{23}Na reaction is negligible compared to the resonant contribution, we have adopted the value of S = 62 keV b = constant from Ref. [53].

RATESMC calculates the lognormal parameters μ and σ that define the reaction rate probability distribution via the relations [44, 61–63]

$$\text{Median Rate} = x_{med} = e^{\mu(T)}, \tag{17}$$

$$\text{Factor Uncertainty} = f.u. = e^{\sigma(T)}. \tag{18}$$

The temperature dependence is explicitly shown here for emphasis. The low and high rates shown in Table VII are given by $e^{\mu(T)-\sigma(T)}$ and $e^{\mu(T)+\sigma(T)}$, respectively, and provide a 68% coverage probability of the reaction rate uncertainty. See Refs. [44, 61–63] for more details on this formalism.

A comparison of ^{22}Ne(p,γ)^{23}Na reaction rate contribution plots calculated using the STARLIB rate (top panel) and the present rate (bottom panel) and is shown in Fig. 18. Note that the 151-keV resonance indicated on Fig. 18 refers to the $3/2^+$ state since the $7/2^-$ upper limit strength contributes very little to the total reaction rate. There are three main points to be seen by Fig. 18. First, the 178-keV resonance is now a significant contributor to the total reaction rate because it is no longer considered an upper limit. Second, the direct-capture rate of Ref. [53] is indeed quite small compared to the new resonant reaction rates of the 151- and 178-keV resonances. Even if the direct-capture rate were increased by the 20% required to account for the increased S(DC→0) indicated in Fig. 11 it would not significantly contribute to the total reaction reaction rate within the Gamow window. Third, the uncertainties in the present reaction rate are much smaller than those using the STARLIB rates, which can be seen in the reduction of the relative widths of these contribution trends.

The fractional uncertainty in our rate as a function of temperature is displayed in Fig. 19. Also shown is the ratio of the pervious STARLIB rate to our present rate (solid blue line) with 1-σ uncertainties in that ratio (dashed blue lines). The present reaction rate is centered at unity. Uncertainties in the present reaction rate are denoted by a continuous red-yellow color gradient with solid, black lines around the present rate indicating 1- and 2-σ uncertainties. Note that the reaction rate at higher energies has increased slightly due to the renormalization of the higher-energy resonance strengths as a consequence of the revised strength for the 458-keV resonance. In fact, because of the new resonance strengths reported here, the reaction rate at $T_9 \approx 0.15$ has increased by approximately a factor of ∼20.

VI. ASTROPHYSICAL IMPACT

Analysis of the astrophysical impact of the present measurements was carried out via Monte Carlo nuclear reaction network calculations exactly as described in Ref. [17] (see also Ref. [65] for a detailed description of this methodology), using the thermally pulsing AGB stellar temperature-density profile of Ref. [16]. The only change from Ref. [17] is that we incorporate our new ^{22}Ne(p,γ)^{23}Na reaction rate. The resulting correlation plots for the final ^{23}Na abundance to the ^{23}Na(p,γ)^{24}Mg, ^{20}Ne(p,γ)^{21}Na, ^{23}Na(p,α)^{20}Ne, and ^{22}Ne(p,γ)^{23}Na reaction rates are shown in Fig. 20. The linear fits to the present correlations are shown in blue and the fits to the correlations presented in Ref. [17] are shown in green. As is discussed in Ref. [17], the x axis of the plots in Fig. 20 is in units of p_i. A positive (negative) p_i value indicates a reaction rate that was p_i lognormal standard deviations above (below) the median rate for a network calculation. Also note that a positive (negative) correlation indicates that a reaction plays a significant role in the production (destruction) of ^{23}Na and also that the uncertainties on the reaction rate are large enough to impact conclusions regarding the ^{23}Na in the relevant astrophysical model. The slope of the correlation between the ^{22}Ne(p,γ)^{23}Na reaction rate and the final ^{23}Na abundance seems to indicate almost no correlation. At the same time, the correlations to the ^{20}Ne(p,γ)^{21}Na and ^{23}Na(p,α)^{20}Ne reactions rates have increased in magnitude, making these reactions even more important to measure.

The average final abundance of ^{23}Na has increased as a result of the measurements made here as well. The final abundance distribution of ^{23}Na before and after these measurements is shown in Fig. 21. The distribution resulting from the Monte Carlo post-processing calculations using the STARLIB rates is shown in blue and the distribution

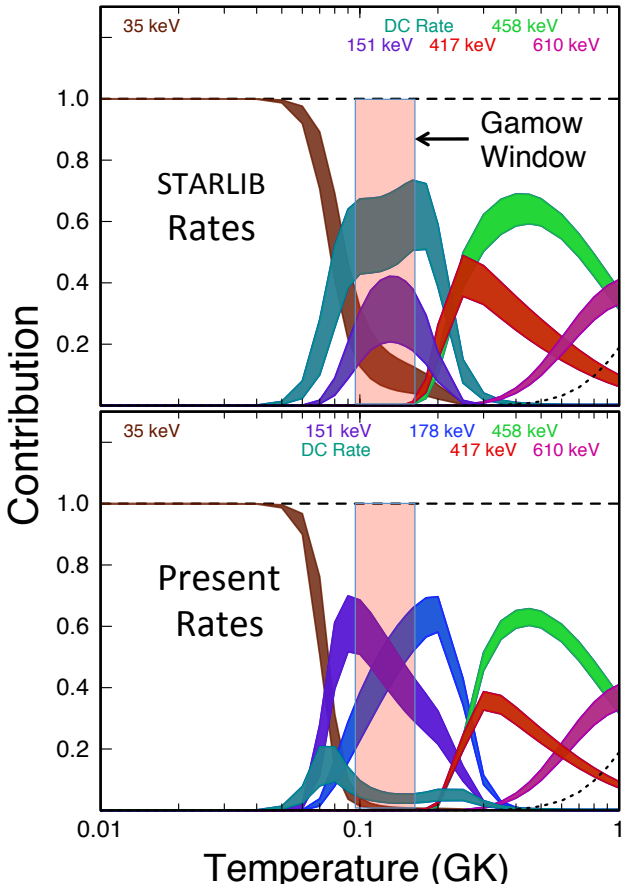

FIG. 18: (color online) A comparison of the reaction rate contribution plot for the ^{22}Ne(p,γ)^{23}Na reaction calculated using the code RATESMC [22, 64] assuming the present rates with the direct-capture cross section of Ref. [53] (bottom panel) to that assuming the STARLIB rates (top panel).

calculated using the present rates is shown in red. The median abundance of the distribution calculated using the present rates is ∼18% higher than the abundance calculated with the STARLIB rates. This ^{23}Na abundance increase is a direct result of the increased ^{22}Ne(p,γ)^{23}Na reaction reported in this work.

This modest increase in ^{23}Na abundance may appear surprising given the drastic increase in the ^{22}Ne(p,γ)^{23}Na reaction rate. Additionally, Ref. [26] recently suggested that their ^{22}Ne(p,γ)^{23}Na reaction rate (which is similar to that measured in this work) should result in an increase in ^{23}Na abundance by a factor of ∼3. However, analysis of the entire NeNa cycle reveals an interesting interplay between the ^{20}Ne(p,γ)^{21}Na and ^{23}Na(p,α)^{20}Ne reactions. The β^+ decays of ^{21}Na and ^{22}Na and proton capture onto ^{21}Ne occur on timescales that are effectively instantaneous compared to the approximately 3×10^3 years between pulses in the AGB model studied here. Furthermore, the mean lifetimes for the ^{20}Ne(p,γ)^{21}Na, ^{22}Ne(p,γ)^{23}Na, and ^{23}Na(p,α)^{20}Ne reactions at the time-weighted average temperature and density of the thermally pulsing AGB stellar model from Ref. [16] ($T_9 = 0.098$ and $\rho = 1.1\times10^{-4}$ g/cm^3) are approximately 1.75×10^5, 9.25×10^3, 1.20×10^3 years, respectively. This implies that the total cycle time is approximately 1.8×10^5 years and is dominated by the slow ^{20}Ne(p,γ)^{21}Na reaction. Additionally, the increased rate of the ^{22}Ne(p,γ)^{23}Na reaction rate allows material to be converted to ^{23}Na earlier, but this ^{23}Na is mostly converted to ^{20}Ne because the ^{23}Na(p,α)^{20}Ne reaction rate is two orders of magnitude faster than the ^{20}Ne(p,γ)^{21}Na rate. It was also suggested in Ref. [66] that the ^{23}Na(p,α)^{20}Ne reaction rate may need to be a factor of 2-4 slower for stellar models to reproduce the observed Na-O anti-correlation, but further measurements of this reaction are required before any definitive conclusions on this topic can be made. Nevertheless, this competition between the ^{20}Ne(p,γ)^{21}Na and ^{23}Na(p,α)^{20}Ne reaction rates determines the final ^{23}Na abundance; therefore, as the correlations in Fig. 20 indicate that further experimental research concerning the Na-O anti-correlation should focus on these reactions.

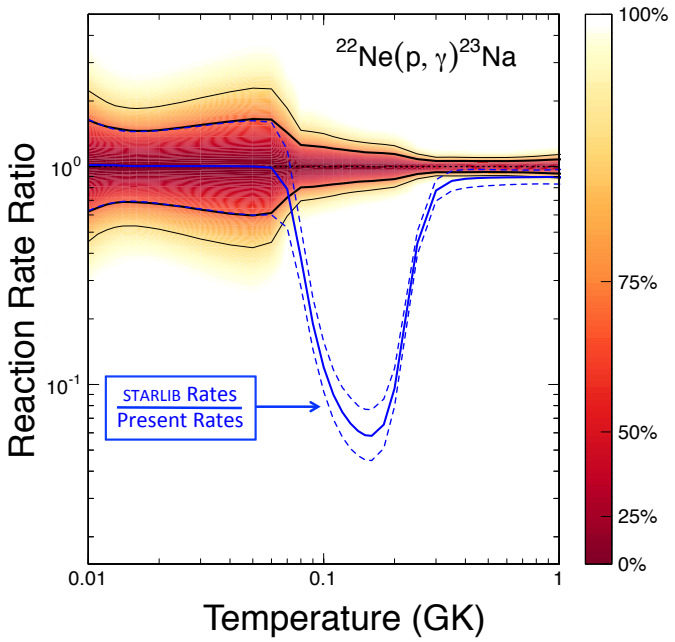

FIG. 19: (color online) The ratio of the STARLIB ^{22}Ne(p,γ)^{23}Na reaction rate to the present rate is shown in blue with dashed blue lines representing 1-σ uncertainties. The present rate is shown centered on the ratio = 1 line in varying shades of red-yellow indicating varying levels of uncertainty in the reaction rate at each temperature.

VII. CONCLUSIONS

Strengths of resonances in the ^{22}Ne(p,γ)^{23}Na reaction at $E_r^{c.m.}$ = 417, 178, & 151 keV and of the direct-capture cross section have been measured relative to the 458-keV resonance in the same reaction. In addition, we have also measured the cross section for the direct-capture process at $E_{c.m.}$ = 407 keV. Several new primary decay branches were identified from the E_x = 9211 keV state, corresponding to the 417-keV resonance, and our measurement of the strength of this resonance is in good agreement with the literature values. We recommended a strength of $\omega\gamma$(417 keV) = 0.082(5) eV. In general, agreement was obtained with the literature DC-model expectations for the direct-capture cross section at lower energies, but further systematic studies are required to determine the origin of the anomalous trend observed from the DC→0 transition as well as the potential transitions that could not be positively identified. Nevertheless, it is clear that such a systematic study would likely not result in a direct-capture reaction rate that contributes significantly to the total reaction rate given the strengths of the 151- and 178-keV resonances reported here.

We measure a resonance strength of $\omega\gamma$(178 keV) = 2.32(32)×10^{-6} eV for the 178-keV resonance, which is just outside of agreement (at the 1-σ level) with the only other direct, definitive measurement of this resonance. However, we report several new primary transitions that were not detected in the previous study [26, 58]. The decays and branching ratios that we measure are consistent with J^π(8972 keV) = 5/2$^+$.

Resonance strengths of $\omega\gamma$(151 keV; 3/2$^+$) = 2.03(40)×10^{-7} eV and $\omega\gamma$(151 keV; 7/2$^-$) ≤ 9.7×10^{-8} eV were measured for the doublet of states assumed to comprise the 151-keV resonance. The strength of the 3/2$^+$ resonance is also just outside of agreement (at the 1-σ level) with the result of Refs. [26, 58]. Although no decay branches could be confidently determined from the 7/2$^-$ state, branching ratios from the 3/2$^+$ state were measured. Despite the fact that the majority of backgrounds in the spectra obtained on these resonances were beam induced, future measurements of both resonances with a more intense proton source could further reduce backgrounds and yield better results.

Nonetheless, our measurements increased the total ^{22}Ne(p,γ)^{23}Na reaction by a factor of ∼20 near the Gamow window for thermally pulsing AGB stars and significantly reduced the reaction rate uncertainties in the same region. Consequently, we estimate an enhancement of approximately 18% in production of ^{23}Na for the particular AGB model used for our network calculations, which is significantly lower than what is suggested in Ref. [26]. This large increase

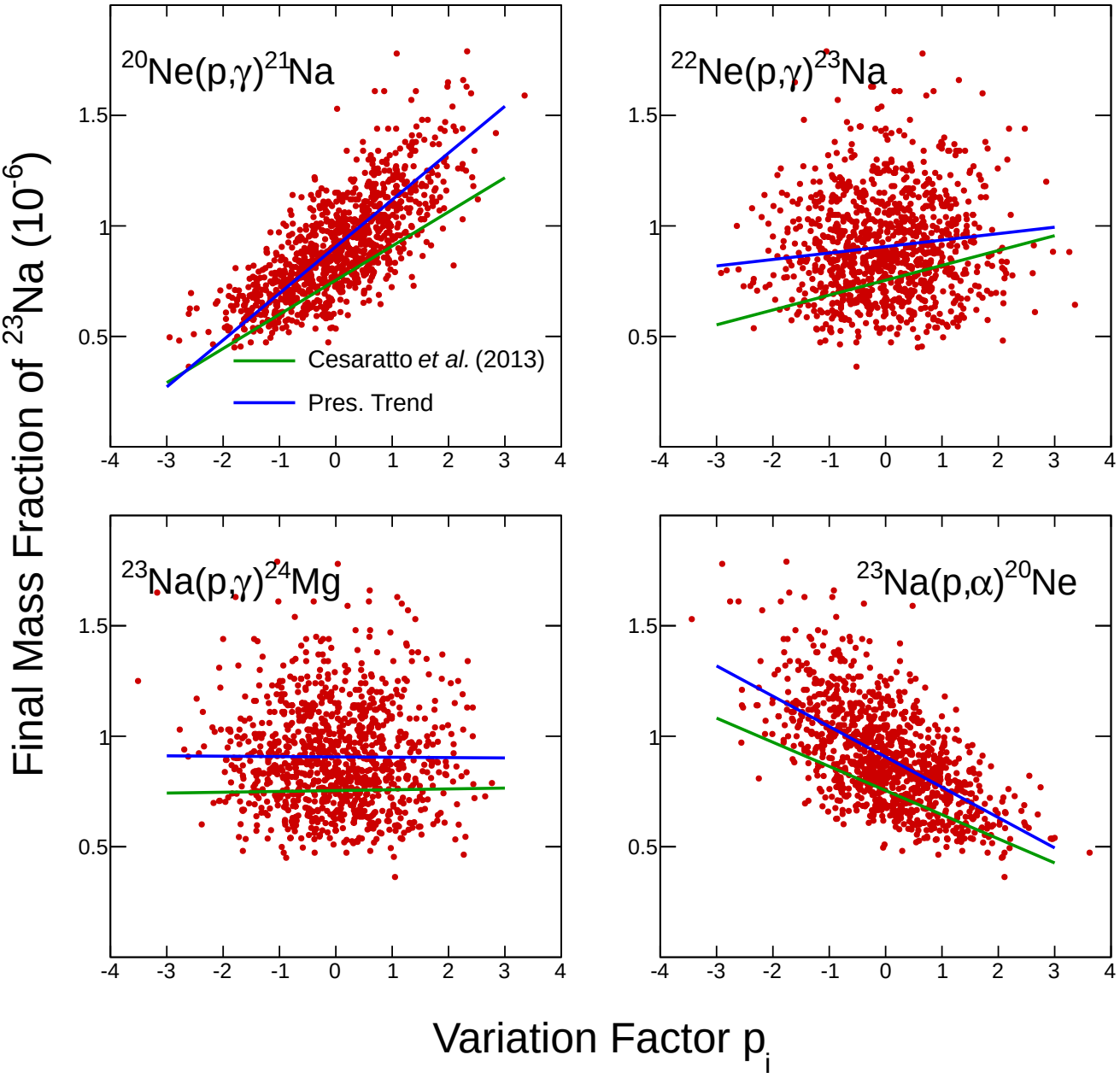

FIG. 20: (color online) Important reaction rates for the production and destruction of ^{23}Na in TP-AGB stars determined after the measurements of the ^{22}Ne(p,γ)^{23}Na reaction rate made for this thesis. Linear fits to the correlation data from Ref. [17] and from the present data are shown in green and blue, respectively.

in the ^{22}Ne(p,γ)^{23}Na reaction rate results in only a modest increase of the ^{23}Na abundance because ^{23}Na is made earlier in the pulse and can therefore be converted more efficiently to ^{20}Ne through ^{23}Na(p,α)^{20}Ne reaction. Finally, future work on this topic should focus on the ^{20}Ne(p,γ)^{21}Na and ^{23}Na(p,α)^{20}Ne reaction rates, which were shown here to be the main sources of uncertainty in the ^{23}Na abundance predicted from thermally pulsing AGB stars.

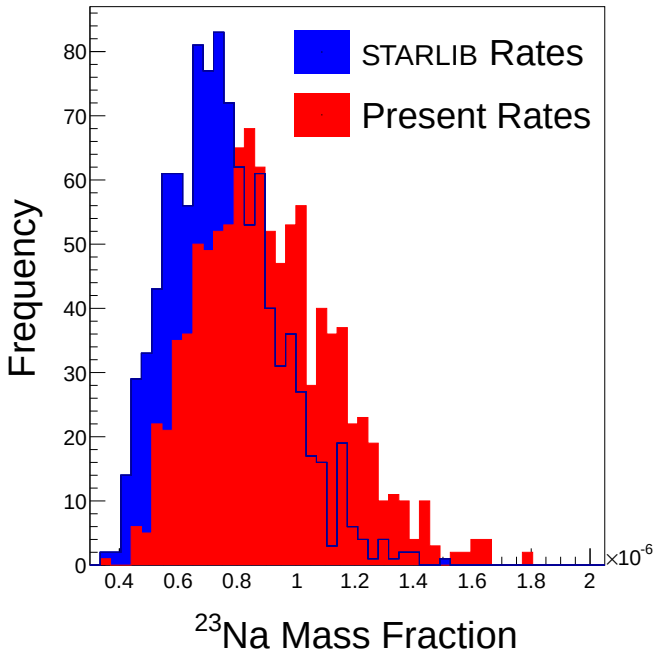

FIG. 21: (color online) The final isotopic abundance distribution of ^{23}Na from Monte Carlo nucleosynthesis network calculations of a 5 $M_\odot$ TP-AGB star before and after the measurements made for this work, shown in blue and red respectively.

ACKNOWLEDGMENTS

This work was supported by the US Department of Energy under grant DE-FG02-97ER41041.

[1] K. M. Ashman and S. E. Zepf, *Globular Cluster Systems* (Cambridge University Press, 1998).
[2] R. G. Gratton, C. Sneden, and E. Carretta, Annu. Rev. Astron. Astr. **42**, 385 (2004).
[3] G. Piotto, L. R. Bedin, J. Anderson, I. R. King, S. Cassisi, A. P. Milone, S. Villanova, A. Pietrinferni, and A. Renzini, Astrophys. J. **661**, L53 (2007).
[4] N. Prantzos and C. Charbonnel, Astron. Astrophys. **458**, 135 (2006).
[5] A. Renzini, Mon. Not. R. Astron. Soc. **391**, 354 (2008).
[6] N. Prantzos, C. Charbonnel, and C. Iliadis, Astron. Astrophys. **470**, 179 (2007).
[7] P. L. Cottrell and G. S. Da Costa, ApJ **245**, L79 (1981).
[8] G. H. Smith and J. Norris, ApJ **254**, 594 (1982).
[9] F. D'Antona, R. Gratton, and A. Chieffi, Mem. Soc. Astron. Italiana **54**, 17 (1983).
[10] P. Ventura, F. D'Antona, I. Mazzitelli, and R. Gratton, Astrophys. J. **550**, L65 (2001).
[11] T. Decressin, G. Meynet, C. Charbonnel, and N. Prantzos, Astron. Astrophys. **464**, 1029 (2007).
[12] S. E. de Mink, O. R. Pols, N. Langer, and R. G. Izzard, Astron. Astrophys. Lett. **507**, 1 (2009).
[13] D. D'Antona and P. Ventura, Mon. Not. R. Astron. Soc. **379**, 1431 (2007).
[14] J.-W. Lee, Mon. Not. R. Astron. Soc. **405**, L36 (2010).
[15] H. J. Habing and H. Olofsson, *Asymptotic Giant Branch Stars* (Springer-Verlag New York Inc., 2004).
[16] P. Ventura and F. D'Antona, Astron. Astrophys. **431**, 279 (2005).
[17] J. M. Cesaratto, A. E. Champagne, M. Q. Buckner, T. B. Clegg, S. Daigle, C. Howard, C. Iliadis, R. Longland, J. R. Newton, and B. M. Oginni, Phys. Rev. C **88**, 065806 (2013).
[18] S. E. Hale, *^{22}Ne(p,γ)^{23}Na, ^{23}Na(p,γ)^{24}Mg, and Globular Cluster Abundance Anomalies*, Ph.D. thesis, University of North Carolina at Chapel Hill (1999).
[19] S. E. Hale, A. E. Champagne, C. Iliadis, V. Y. Hansper, D. C. Powell, and J. C. Blackmon, Phys. Rev. C **65**, 015801 (2001).

[20] P. M. Endt, Nucl. Phys. A **521**, 1 (1990).
[21] D. G. Jenkins, M. Bouhelal, S. Courtin, M. Freer, B. R. Fulton, F. Haas, R. V. F. Janssens, T. L. Khoo, *et al.*, Phys. Rev. C **87**, 064301 (2013).
[22] C. Iliadis, R. Longland, A. E. Champagne, A. Coc, and R. Fitzgerald, Nucl. Phys. A **841**, 31 (2010).
[23] R. B. Firestone, Nucl. Data Sheets **108**, 1 (2007).
[24] F. Cavanna, R. Depalo, M.-L. Menzel, M. Aliotta, M. Anders, D. Bemmerer, *et al.*, Eur. Phys. J. A **50**, 179 (2014).
[25] `http://www.nndc.bnl.gov/ensdf/`.
[26] F. Cavanna, R. Depalo, M. Aliotta, M. Anders, D. Bemmerer, A. Best, *et al.*, Phys. Rev. Lett. **115**, 252501 (2015).
[27] R. Barlow and C. Beeston, Comp. Phys. Commun. **77**, 219 (1993).
[28] R. Brun and F. Rademakers, Nucl. Instrum. Methods A **389**, 81 (1997).
[29] J. Dermigny, C. Iliadis, M. Q. Buckner, K. J. Kelly, A. E. Champagne, *et al.*, Nucl. Instrum. and Methods A **830**, 427 (2016).
[30] K. J. Kelly, A. E. Champagne, R. Longland, and M. Q. Buckner, Phys. Rev. C **92**, 035805 (2015).
[31] R. Depalo, F. Cavanna, F. Ferraro, S. Alessandra, T. Al-Abdullah, S. Akhmadaliev, *et al.*, Phys. Rev. C **92**, 045807 (2015).
[32] M. Q. Buckner, C. Iliadis, K. J. Kelly, L. N. Downen, A. E. Champagne, J. M. Cesaratto, C. Howard, and R. Longland, Phys. Rev. C **91**, 015812 (2015).
[33] J. M. Cesaratto, A. E. Champagne, T. B. Clegg, M. Q. Buckner, R. C. Runkle, and A. Stefan, Nucl. Instrum. and Methods A **623**, 888 (2010).
[34] M. Q. Buckner, C. Iliadis, J. M. Cesaratto, C. Howard, T. B. Clegg, A. E. Champagne, and S. Daigle, Phys. Rev. C **86**, 065804 (2012).
[35] C. Howard, C. Iliadis, and A. E. Champagne, Nucl. Instrum. and Methods A **729**, 254 (2013).
[36] K. B. Swartz, D. W. Visser, and J. M. Baris, Nucl. Instrum. Methods A **463**, 354 (2001).
[37] S. Carson, C. Iliadis, J. M. Cesaratto, A. E. Champagne, L. N. Downen, M. Ivanovic, J. Kelley, R. Longland, J. R. Newton, G. Rusev, and A. P. Tonchev, Nucl. Instrum. Methods A **618**, 190 (2010).
[38] R. Longland, C. Iliadis, A. E. Champagne, C. Fox, and J. R. Newton, Nucl. Instrum. and Methods A **566**, 452 (2006).
[39] K. J. Kelly, *Nuclear Reaction Rate Uncertainties and the $^{22}Ne(p,\gamma)^{23}Na$ Reaction Rate: Classical Novae and Globular Clusters*, Ph.D. thesis, University of North Carolina at Chapel Hill (2016).
[40] D. Vermilyea, Acta Metallurgica **1**, 282 (1953).
[41] M. Mayer, J. L. Duggan, and I. L. Morgan, in *SIMNRA, a Simulation Program for the Analysis of NRA, RBS, and ERDA, Proc. 15th International Conference on the Application of Accelerators in Research and Industry* (Denton, TX, 1998).
[42] C. Iliadis, *Nuclear Physics of Stars, 2^{nd} Ed.* (Wiley-VCH Verlag GmbH and Co. KGaA Weinheim, 2015).
[43] J. F. Ziegler and J. P. Biersack, (unpublished) (2003).
[44] R. Longland, C. Iliadis, J. M. Cesaratto, A. E. Champagne, S. Daigle, J. R. Newton, and R. Fitzgerald, Phys. Rev. C **81**, 055804 (2010).
[45] M. Q. Buckner, *Hydrogen Burning of the Rare Oxygen Isotopes*, Ph.D. thesis, University of North Carolina at Chapel Hill (2015).
[46] S. Agostinelli, J. Allison, K. Amako, J. Apostolakis, H. Araujo, and P. Arce, Nucl. Instrum. and Methods A **506**, 250 (2003).
[47] L. C. Biedenharn and M. E. Rose, Rev. Mod. Phys. **25** (1953).
[48] F. James and M. Roos, Comp. Phys. Commun. **10**, 343 (1988).
[49] R. Runkle, *A New Measurement of the Fusion Reaction $^{14}N(p,\gamma)^{15}O$ and Its Impact On Hydrogen Burning, Globular Clusters, and the Age of the Universe*, Ph.D. thesis, University of North Carolina at Chapel Hill (2003).
[50] M. A. Meyer and J. J. A. Smit, Nucl. Phys. A **205**, 177 (1973).
[51] Z. B. du Toit, P. R. de Kock, and W. L. Mouton, Z. Physik **246**, 170 (1971).
[52] J. Keinonen, M. Riihonen, and A. Anttila, Nucl. Instrum. and Methods **15**, 579 (1977).
[53] J. Görres, H. W. Becker, L. Buchmann, C. Rolfs, P. Schmalbrock, H. P. Trautvetter, A. Vlieks, J. W. Hammer, and T. R. Donoghue, Nucl. Phys. A **408**, 372 (1983).
[54] C. Rolfs, W. S. Rodney, M. H. Shapiro, and H. Winkel, Nucl. Phys. A **241**, 3 (1975).
[55] W. H. Hietzke, Ph.D. thesis, California State University (1975).
[56] T. Ericson, Phys. Rev. Lett. **5**, 430 (1960).
[57] M.-L. Menzel, *Experimental Study of the $^{22}Ne(p,\gamma)^{23}Na$ Reaction and its Implications for Novae Scenarios*, Master's thesis, "Technische Universität Dresden" (2013).
[58] R. Depalo, F. Cavanna, M. Aliotta, M. Anders, D. Bemerrer, A. Best, *et al.*, Phys. Rev. C **94**, 055804 (2016).
[59] J. R. Powers, H. T. Fortune, and R. Middleton, Phys. Rev. C **4**, 2030 (1971).
[60] W. A. Childs, R. C. Ritter, B. D. Murphy, and R. M. Strang, Nucl. Phys. A **203**, 133 (1973).
[61] A. L. Sallaska, C. Iliadis, A. E. Champagne, S. Goriely, S. Starrfield, and F. X. Timmes, Astrophys. J. Supp. **207**, 18 (2013).
[62] K. J. Kelly, C. Iliadis, L. N. Downen, J. José, and A. E. Champagne, ApJ **777**, 130 (2013).
[63] C. Iliadis, R. Longland, A. Coc, F. X. Timmes, and A. E. Champagne, J. Phys. G **42**, 034007 (2015).
[64] R. Longland, C. Iliadis, A. E. Champagne, J. R. Newton, and C. Ugalde, Nucl. Phys. A **841**, 1 (2010b).
[65] R. Longland, Astron. Astrophys. **548**, A30 (2012).
[66] P. Ventura and F. D'Antona, Astron. Astrophys. **457**, 995 (2006).

Appendix A: Numerical Table of the ^{22}Ne(p,γ)^{23}Na Thermonuclear Reaction Rate

T(GK)	Low Rate	Median Rate	High Rate	Lognormal μ	Lognormal σ	A-D Statistic
0.010	4.16×10^{-25}	6.68×10^{-25}	1.09×10^{-24}	-5.566×10^{1}	4.84×10^{-1}	4.38×10^{-1}
0.011	1.57×10^{-23}	2.42×10^{-23}	3.80×10^{-23}	-5.207×10^{1}	4.41×10^{-1}	5.23×10^{-1}
0.012	3.21×10^{-22}	4.79×10^{-22}	7.30×10^{-22}	-4.909×10^{1}	4.13×10^{-1}	5.40×10^{-1}
0.013	4.04×10^{-21}	5.91×10^{-21}	8.87×10^{-21}	-4.657×10^{1}	3.94×10^{-1}	6.12×10^{-1}
0.014	3.49×10^{-20}	5.07×10^{-20}	7.50×10^{-20}	-4.443×10^{1}	3.84×10^{-1}	6.15×10^{-1}
0.015	2.23×10^{-19}	3.24×10^{-19}	4.74×10^{-19}	-4.257×10^{1}	3.78×10^{-1}	5.50×10^{-1}
0.016	1.12×10^{-18}	1.63×10^{-18}	2.38×10^{-18}	-4.096×10^{1}	3.77×10^{-1}	5.27×10^{-1}
0.018	1.62×10^{-17}	2.38×10^{-17}	3.47×10^{-17}	-3.828×10^{1}	3.82×10^{-1}	7.23×10^{-1}
0.020	1.34×10^{-16}	1.99×10^{-16}	2.93×10^{-16}	-3.616×10^{1}	3.92×10^{-1}	9.63×10^{-1}
0.025	5.69×10^{-15}	8.68×10^{-15}	1.31×10^{-14}	-3.238×10^{1}	4.21×10^{-1}	1.10×10^{0}
0.030	6.51×10^{-14}	1.03×10^{-13}	1.59×10^{-13}	-2.991×10^{1}	4.48×10^{-1}	1.09×10^{0}
0.040	1.25×10^{-12}	2.05×10^{-12}	3.31×10^{-12}	-2.692×10^{1}	4.88×10^{-1}	9.75×10^{-1}
0.050	6.95×10^{-12}	1.16×10^{-11}	1.93×10^{-11}	-2.518×10^{1}	5.09×10^{-1}	6.93×10^{-1}
0.060	2.33×10^{-11}	3.80×10^{-11}	6.25×10^{-11}	-2.399×10^{1}	4.90×10^{-1}	4.38×10^{-1}
0.070	9.59×10^{-11}	1.33×10^{-10}	1.90×10^{-10}	-2.273×10^{1}	3.45×10^{-1}	8.28×10^{0}
0.080	7.22×10^{-10}	9.00×10^{-10}	1.13×10^{-9}	-2.082×10^{1}	2.27×10^{-1}	1.38×10^{0}
0.090	5.72×10^{09}	7.08×10^{-9}	8.79×10^{-9}	-1.876×10^{1}	2.18×10^{01}	2.97×10^{0}
0.100	3.53×10^{-8}	4.31×10^{-8}	5.29×10^{-8}	-1.696×10^{1}	2.05×10^{-1}	1.97×10^{0}
0.110	1.64×10^{-7}	1.97×10^{-7}	2.39×10^{-7}	-1.544×10^{1}	1.90×10^{-1}	8.97×10^{-1}
0.120	5.95×10^{-7}	7.11×10^{-7}	8.51×10^{-7}	-1.415×10^{1}	1.78×10^{-1}	6.68×10^{-1}
0.130	1.79×10^{-6}	2.12×10^{-6}	2.51×10^{-6}	-1.306×10^{1}	1.68×10^{-1}	4.62×10^{-1}
0.140	4.61×10^{-6}	5.41×10^{-6}	6.35×10^{-6}	-1.213×10^{1}	1.61×10^{-1}	3.06×10^{-1}
0.150	1.05×10^{-5}	1.22×10^{-5}	1.42×10^{-5}	-1.131×10^{1}	1.55×10^{-1}	1.84×10^{-1}
0.160	2.14×10^{-5}	2.49×10^{-5}	2.89×10^{-5}	-1.060×10^{1}	1.50×10^{-1}	1.45×10^{-1}
0.180	7.09×10^{-5}	8.16×10^{-5}	9.41×10^{-5}	-9.413×10^{0}	1.42×10^{-1}	1.09×10^{-1}
0.200	1.89×10^{-4}	2.16×10^{-4}	2.46×10^{-4}	-8.440×10^{0}	1.33×10^{-1}	1.79×10^{-1}
0.250	1.86×10^{-3}	2.01×10^{-3}	2.18×10^{-3}	-6.207×10^{0}	7.94×10^{-2}	8.76×10^{-1}
0.300	2.24×10^{-2}	2.38×10^{-2}	2.53×10^{-2}	-3.737×10^{0}	5.97×10^{-2}	3.54×10^{-1}
0.350	1.85×10^{-1}	1.97×10^{-1}	2.09×10^{-1}	-1.627×10^{0}	6.07×10^{-2}	3.07×10^{-1}
0.400	9.55×10^{-1}	1.01×10^{0}	1.07×10^{0}	1.260×10^{-2}	6.01×10^{-2}	2.63×10^{-1}
0.450	3.46×10^{0}	3.67×10^{0}	3.89×10^{0}	1.301×10^{0}	5.88×10^{-2}	2.77×10^{-1}
0.500	9.78×10^{0}	1.04×10^{1}	1.10×10^{1}	2.337×10^{0}	5.80×10^{-2}	2.63×10^{-1}
0.600	4.70×10^{1}	4.99×10^{1}	5.29×10^{1}	3.910×10^{0}	5.85×10^{-2}	3.81×10^{-1}
0.700	1.47×10^{2}	1.57×10^{2}	1.67×10^{2}	5.054×10^{0}	6.17×10^{-2}	7.13×10^{-1}
0.800	3.53×10^{2}	3.77×10^{2}	4.03×10^{2}	5.933×10^{0}	6.61×10^{-2}	1.04×10^{0}
0.900	7.08×10^{2}	7.60×10^{2}	8.16×10^{2}	6.634×10^{0}	7.09×10^{-2}	1.32×10^{0}
1.000	1.25×10^{3}	1.35×10^{3}	1.46×10^{3}	7.209×10^{0}	7.55×10^{-2}	1.47×10^{0}
1.250	3.64×10^{3}	3.95×10^{3}	4.31×10^{3}	8.284×10^{0}	8.54×10^{-2}	2.15×10^{0}
1.500	7.64×10^{3}	8.35×10^{3}	9.18×10^{3}	9.033×10^{0}	9.28×10^{-2}	3.12×10^{0}
1.750	1.32×10^{4}	1.45×10^{4}	1.60×10^{4}	9.583×10^{0}	9.73×10^{-2}	4.33×10^{0}
2.000	2.00×10^{4}	2.20×10^{4}	2.44×10^{4}	1.000×10^{1}	9.96×10^{-2}	5.32×10^{0}
2.500	3.61×10^{4}	3.97×10^{4}	4.40×10^{4}	1.059×10^{1}	9.95×10^{-2}	6.78×10^{0}
3.000	5.35×10^{4}	5.86×10^{4}	6.48×10^{4}	1.098×10^{1}	9.66×10^{-2}	7.57×10^{0}
3.500	7.03×10^{4}	7.68×10^{4}	8.45×10^{4}	1.125×10^{1}	9.27×10^{-2}	7.75×10^{0}
4.000	8.56×10^{4}	9.31×10^{4}	1.02×10^{5}	1.145×10^{1}	8.89×10^{-2}	8.06×10^{0}

TABLE VII: Numerical table of the total thermonuclear ^{22}Ne(p,γ)^{23}Na reaction rate, in cm^3 mol^{-1} s^{-1}, after the measurements made for this thesis. The tabulated reaction rate includes the direct-capture contribution of Ref. [53]. The code RATESMC was used to calculate the reaction rate at each temperature. The column labeled "A-D Statistic" refers to the Anderson-Darling statistic associated with the assumption of a lognormally distributed reaction rate. Generally, an A-D statistic less than ≈ 1 indicates that the reaction rate distribution at that temperature is well described by the assumed lognormal distribution. However, the lognormally-distributed reaction rate assumption still holds for an A-D statistic in the range of $\approx$ 1-30 [22]. The lognormal parameters μ and σ describe the reaction rate probability distribution function as discussed in the text.